2-21-2012

Intermittently Forced Vortex Rossby Waves

Amaryllis Cotto
Florida International University, acott002@fiu.edu

DOI: 10.25148/etd.FI12041105

FLORIDA INTERNATIONAL UNIVERSITY

Miami, Florida

INTERMITTENTLY FORCED VORTEX ROSSBY WAVES

A thesis submitted in partial fulfillment of the

requirements for the degree for the degree of

MASTER OF SCIENCE

in

GEOSCIENCE

by

Amaryllis Cotto

2012

To: Dean Kenneth G. Furton
College of Arts and Science

This thesis, written by Amaryllis Cotto, and entitled Intermittently Forced Vortex Rossby Waves, having been approved in respect to style and intellectual content, is referred to you for judgment.

We have read this thesis and recommend that it be approved.

_____
Haiyan Jiang

_____
Ping Zhu

_____
Hugh Willoughby, Major Professor

Date of Defense: February 21, 2012

The thesis of Amaryllis Cotto is approved.

_____
Dean Kenneth G. Furton
College of Arts and Science

_____
Dean Lakshmi N.Reddi
University Graduate School

Florida International University, 2012

DEDICATION

I would like to dedicate this research to my family, who love me unconditionally and support me through the good and bad times. Thank you for your unending encouragement, faith, and love.

ACKNOWLEDGMENTS

My sincerest gratitude goes to my thesis advisor; Dr. Hugh Willoughby, who has supported me with his knowledge and guidance. I would like to thank him for his insight and most importantly, for his patience with this research and my thesis writing. My master's degree as well as my thesis would have never been possible without his assistance and direction. I also thank him for all the Mat Lab teaching sessions, which allowed me to learn and embrace the beauty of the language and for sharing his love for meteorology and his "gifted intellect."

I would like to thank my thesis committee members, Dr. Ping Zhu and Dr. Haiyan Jiang for their support, recommendation, and suggestions. A special thanks to my colleagues and friends: Joseph Zagrodnik and Corey Walton, for looking out for me and helping me survive the thesis writing, for aiding my mental and physical health, and for their friendship and support.

I am heartily thankful to my loved ones for all their love and support. I thank my mother for being my best friend and counselor, for encouraging me no matter how crazy my ideas are or how hectic my lifestyle is, for her unbending faith, and for always picking me up after I fall. I thank my father for his strength and determination and teaching me how important they are in life, for encouraging me and allowing me to fulfill my dreams, and for being my role model. To my sisters for always being there for me, for all the sister talks and advise, and for never putting me down. I thank Naaman Beck for all his love and support, for sticking through the hard times, for encouraging and supporting my wild ideas and lifestyle, and for making me feel so special and beautiful.

This research was supported financially by the National Science Foundation (ATM0454501) and the facilities and materials were provided by Florida International University.

ABSTRACT OF THE THESIS

INTERMITTENTLY FORCED VORTEX ROSSBY WAVES

by

Amaryllis Cotto

Florida International University, 2012

Miami, Florida

Professor Hugh Willoughby, Major Professor

Wavelike spiral asymmetries are an intriguing aspect of Tropical Cyclone dynamics. Previous work hypothesized that some of them are Vortex Rossby Waves propagating on the radial gradient of mean–flow relative vorticity. In the Intermittently Forced Vortex Rossby Wave theory, intermittent convection near the eyewall wind maximum excites them so that they propagate wave energy outward and converge angular momentum inward. The waves' energy is absorbed as the perturbation vorticity becomes filamented near the outer critical radii where their Doppler–shifted frequencies and radial group velocities approaches zero. This process may initiate outer wind maxima by weakening the mean–flow just inward from the critical radius. The waves are confined to a relatively narrow annular waveguide because of their slow tangential phase velocity and the narrow interval between the Rossby wave cut–off frequency, where the radial wavenumber is locally zero, and the zero frequency, where it is locally infinite.

TABLE OF CONTENTS

LIST OF FIGURES

INTRODUCTION

Theoretical Vortex Rossby waves (VRWs) resemble observed spiral bands in hurricanes. Previous studies were based upon analytical solutions with idealized mean flows. This research offers a numerical perspective that is computationally and conceptually simpler.

The solution's vorticity fields are narrow, relatively tightly wound spirals, consistent with earlier works. By contrast, the streamfunction and geopotential form broad more-or-less circular gyres. Propagating VRWs exist in an annular waveguide bounded by an inner radius where the waves frequency is Doppler shifted to the Rossby-wave cut off frequency and an outer radius where it is Doppler shifted to zero and the waves are absorbed. They transport vorticity and wave energy outward and angular momentum inward.

TROPICAL CYCLONES

PHYSICAL PROPERTIES

Tropical Cyclones are counterclockwise rotating (in the Northern Hemisphere) convective vortices formed from pre-existing disturbances (such as African easterly waves) over ocean waters warmer than 26° C. They are warm-core systems that move as a coherent objects and evolve slowly on times scaled by the orbital period of air circulating around the center. The eye contains low central pressure, calm winds at its center, and a few low-level clouds. The eyewall encompasses the radius of maximum winds (RMW) and is characterized by deep convective clouds that extend to the tropopause. Around the eye, spiral rain bands rotate cyclonically at a speed slower than the tangential wind (e.g., MacDonald 1968; Willoughby, 1988; Montgomery and Kallenbach, 1997).

SPIRAL RAIN BANDS

Spiral rain bands are elongated strands of precipitating clouds and convection. They rotate cyclonically within the hurricane and wrap around the vortex. Depending upon the size of the vortex itself, these bands can extend hundreds of kilometers from the eyewall (Romine and Wilhelmson 2006). Geometrically they can be represented as trailing equiangular spirals (Senn and Hiser 1959). They appear to propagate outward as they are advected cyclonically downwind by the axially symmetric mean flow with velocities lower than the mean tangential wind. One

theory of their genesis is linked to energy released by the exchange of potential vorticity anomalies within the symmetric vortex (e.g., Guinn and Schubert 1993). Accordingly, spiral bands can be interpreted as Vortex Rossby Waves.

MacDonald (1968) first suggested that spiral rain bands in hurricanes are Rossby waves that propagate upstream upon the negative radial gradient of mean-vortex relative vorticity. McDonald's interpretation is analogous to mid-latitude Rossby wave propagation on the meridional gradient of planetary vorticity. The Rossby wave hypothesis was supported because the spiral bands tilt upstream, move more slowly than the mean wind, and convective cells advect through the bands. Quantitatively, if Rossby waves are present, then they should transport angular momentum inward and wave energy outward. In the beginning of the Vortex Rossby Wave theory, these ideas were hard to verify because of poor quality of aircraft data and because cells in the spiral bands continuously grew and dissipated.

Alternatively, Willoughby (1977, 1978) proposed that spiral bands are inward propagating inertia-buoyancy (IB) waves. Simulated bands in this model exhibited transport of energy towards the center of the vortex and outward transport of angular momentum. The wave phase propagation was upstream, against the mean flow, slower than the mean flow (like Rossby waves), so that the waves were advected downstream. If the cyclone was strong enough (maximum velocity > 50 ms^{-1}), IB waves could be Doppler shifted to the Brunt Väisälä (Buoyancy) frequency. At the critical radius, where their intrinsic frequency was Doppler shifted to the Buoyancy frequency, the horizontal wavenumber became locally infinite and the waves were absorbed. Willoughby (personal communication) initially attempted to

apply this line of reasoning to VRWs but was unable to simulate narrow trailing spirals that extended over substantial radial intervals. Slow intrinsic phase propagation was a key obstacle.

In the Intermittently Forced Vortex Rossby wave analysis, the VRWs' are confined in a waveguide between the cut-off frequency radius and the critical radius, where the frequency is Doppler-shifted to zero. The waveguide is the only area where the VRWs can propagate and transfer wave energy and angular momentum radially. The critical radius phenomenon, which is not clearly discussed in previous literature, can be understood by analogy with the IB waves' critical radius their frequencies are Doppler-shifted to the Brunt Väisälä frequency (Willoughby 1977).

DYNAMIC AND THERMODYNAMIC PROPERTIES: SOME THEORIES OF INTENSIFICATION AND WEAKENING

Heat and angular momentum sources influence symmetric vortex behavior. The dominant control of TC intensity is the oceanic energy source. The symmetric response to convective latent heat release is constrained by thermodynamic stability, inertial stability and baroclinicity. Surface frictional convergence of moist enthalpy in the boundary layer feeds cumulus clouds that release latent heat into the free atmosphere in the vortex core. Convective heating is generally strongest in the eyewall where it forces mean ascent, deep convergence in the lower troposphere, and outflow in the upper troposphere. The outward flowing air eventually sinks because of adiabatic cooling at larger radius. This secondary circulation is characterized by

convergence in and just above the boundary layer, upward vertical motion coincident with the eyewall heat source, upper divergence, and downward vertical motion far from the center.

The thermodynamic stability is essentially fixed; however, inertial stability and baroclinicity vary spatially and temporally as the vortex intensity changes. Baroclinicity constricts the motions due to the heat source near the radius of maximum winds. It allows inflow to penetrate past the RMW into the strong vorticity of the eyewall, leading to vortex intensification. Inertial stability localizes the frictional convergence beneath the eyewall, focusing latent heat release inside the radius of maximum winds. The eye has the strongest inertial stability because the tangential wind increases outward so that the angular momentum has a sharp radial gradient. Where the gradient of angular momentum is tight, the vortex is very inertially stable. Therefore, the vortex intensifies because latent heat release forces vertical motion that, in turn, produces strong radial motions across the tight gradients. The high values of inertial stability concentrate vertical motions just inside the RMW (Eliassen, 1952; Shapiro and Willoughby, 1982; Schubert and Hack, 1982; Pendergrass and Willoughby, 2009).

PREVIOUS WORKS

INTRODUCTION TO VRW THEORY

Guinn and Schubert (1993) analyzed Rossby wave characteristics and the relationship between spiral bands and the potential vorticity (PV) field. Friction and mass sources or sinks were neglected in their *f*-plane, shallow water PV model. Their waves propagated on a circular, piecewise continuous distribution of mean-vortex PV, such that PV perturbations appeared as undulations of the boundaries. By analogy with the general circulation, PV contours assumed sinusoidal wave patterns; centers of positive and negative PV propagated upwind (westward in the general circulation case). In a "Surf Zone," where the PV gradients were relatively weak, the radial group propagation slowed, resulting in accumulation of wave energy and wave breaking. There, spiral bands became filamented and transferred their PV to the mean flow. In reality, the waves simulated in this model were strictly linear, thus, they did not break. Instead, wave energy accumulated in the surf zone where both the Doppler-shifted frequency and radial group velocity approached zero. Ultimately, the model's Newtonian friction absorbed the waves.

Shapiro and Montgomery (1993) used the asymmetric balance theory (AB) to model wave properties in hurricanes. It is the high Rossby number analog to the synoptic-scale quasigeostrophic formulation. The AB approximation, in which the second time derivative was assumed to be slow compared with the square of inertia frequency, allowed for balanced-wind calculations at large Rossby numbers. It also

allowed for divergent perturbations, whose radial wavenumber increased with time as wave packets propagated across the radially shearing mean flow, and energy transferred from the asymmetric flow to the axially symmetric vortex.

The Eliassen Palm (1960) Theorem (EPT) was originally developed in a quasigeostrophic context to describe synoptic-scale flows in geostrophic and hydrostatic balance. As re-derived for the hurricane case, the EPT describes variations of radial eddy fluxes of wave energy and angular momentum that interact with the mean flow only where the waves are forced or where they experience critical-surface absorption (McIntyre 1977, Andrews and McIntyre 1978a, 1978b, Boyd 1977).

Montgomery and Kallenbach (1997) analyzed vorticity-wave structure of spiral bands that propagated outward and moved more slowly than that of the mean tangential wind. These VRWs exhibited the same characteristics identified by MacDonald (1968). The AB theory filtered out gravity and inertial waves. With zero heating or friction, wave propagation depended entirely upon conservation of potential vorticity. The Wentzel Kramers Brillouin (WKB) theory was used to compute the waves' structure in both Rankine-like and continuous vortices. Energy and momentum transferred from asymmetric potential vorticity anomalies to the symmetric parts of mean flow could force mean-vortex intensity changes over time (Montgomery and Enagonio 1998). In the continuous-vortex wavenumber-one version of the problem, the vortex center was displaced and the circulation intensified as an initial wavenumber-one PV anomaly became symmetrized. During

this process, the asymmetric PV became wrapped around the vortex in increasingly tightly-wound spiral filaments.

Möller and Montgomery (1999, 2000) confirmed intensification through incorporation of initial PV anomalies into axially symmetric shallow-water and three-dimensional baroclinic vortices. A key common factor in the work of Guinn and Schubert (1993) and Montgomery and his coauthors was formulation as an initial value problem in which a preexisting PV distribution evolved dynamically. In Guinn and Schubert (1993), outward diffusion from the high PV core became filamented into spiral bands. In Montgomery and coauthors' work, the net cyclonic part of initial PV distribution became incorporated into the axially symmetric vortex, resulting in mean-flow intensification as the asymmetric PV filamented. Subsequent analyses (Hendricks et al. 2004 and Montgomery et al. 2006) of full-physics numerical simulations extended the latter paradigm to include convective generation of the PV anomaly.

Asymmetric balance is not strictly applicable for wavenumbers less than 1. For example, wavenumber 2 instabilities do indeed exist (Terwey and Montgomery 2002); however, their impact on the vortex is poorly understood. In an alternative to WKB or piecewise continuous analyses, Willoughby (1978), treated TC asymmetries as continuous trains of forced IB waves that conserved the tangential wavenumber and the apparent frequency (with respect to the ground) of the forcing as they propagated radially. This research combines these approaches through Fourier synthesis of a spectrum of intermittently forced waves.

The hypothesis that spiral bands are VRWs that propagate on the radial gradient of mean-flow relative vorticity has appealing aspects. They are advected downwind as a train of cyclonic and anticyclonic vortices moving around the vortex with less than the mean tangential wind speed. VRWs also propagate wave energy outward, even though their radial phase velocity is directed inward. Their Doppler-shifted frequencies lie between the Rossby-wave cutoff frequency and zero. If they are excited near the radius of maximum wind, the waves should transport angular momentum inward toward the locus of forcing and carry wave energy outward toward the critical radius. The wave energy is absorbed as the Doppler-shifted frequency approaches zero. There, cyclonic (positive) and anticyclonic (negative) vorticity filaments become so elongated that their influences mask each other in Poisson-equation inversions to obtain the streamfunction or geopotential. The group velocity approaches zero so that the waves cannot propagate past the critical radius.

SPIRAL BANDS AND NUMERICAL MODELING

Inner and outer spiral rain bands are distinctive features of hurricane imagery. Numerical simulations seem to link their properties to Vortex Rossby waves. Extending the synthesis of Willoughby et al. (1984b) and Willoughby (1988), Houze (2010) studied separate categories of spiral rainbands: Distant rainbands, the primary rainband, and secondary rainbands. The distant rainbands form far from the storm center outside the vortex core. They are not considered VRWs since the mean-flow radial vorticity gradient there is so weak. The primary rainband is within the vortex core; however, it does not appear to be a Vortex Rossby wave. Secondary

rainbands are spiral bands, smaller than the primary rainband, with Rossby wave-like radial and azimuthal propagation. Radar observations (Reasor et al 2000 and Corbosier et al 2006) confirmed that secondary rainbands have properties consistent with Vortex Rossby wave.

In contrast with the vorticity perturbations considered previously, Nolan and Montgomery (2002) and Nolan and Grasso (2003) initialized perturbations on symmetric vortices as asymmetric and symmetric initial thermal anomalies. The adjustment process occurred in two stages: adjustment to balance and axisymmetrization of the resulting vorticity perturbation. Asymmetric thermal perturbations weakened the mean vortex in most cases; whereas symmetric thermal perturbations strengthened it, but only about as much as would be expected from a balanced response to the heat added.

The airborne dual-Doppler radar data from Hurricane Olivia of 1994 (Figure 1) established a connection between asymmetric dynamics and observational data (Reasor et al. 2000 and Black et al. 2002). Within Olivia's vortex, spiral bands of vorticity were located near the 20 km radius; deep convection in the eyewall may have forced VRWs, leading to outward energy fluxes and inward momentum fluxes consistent with the EP Theorem. However, there were many factors, such as local vertical shear, that could have contributed to the storms intensity changes and it was not apparent that these features alone caused the vortex to spin up. These wavenumber 2 barotropic non-divergent VRWs resemble observed spiral bands in hurricane Olivia, as discussed in the Appendix.

Hurricane Olivia 1994

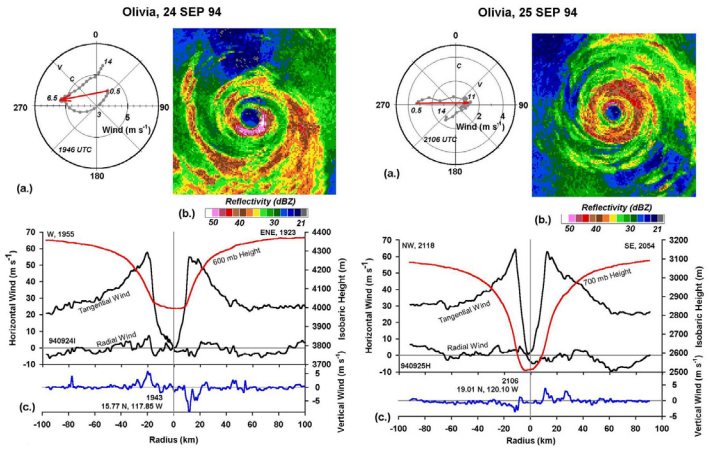

Figure 1: Vertical and horizontal profiles of Hurricane Olivia (1994) on September 24 and 25 (Black et al. 2002).

The Pennsylvania State University-National Center for Atmospheric Research Model Version 5 (PSU-NCAR MM5) is a non-hydrostatic mesoscale model that can simulate TC spiral PV bands on a high-resolution grid (Chen and Yau 2001). A 24hr numerical simulation reproduced formation of spiral bands observed during the first stage of Hurricane Andrew's rapid deepening. Analysis of the rain bands, latent heat release, and PV anomalies suggested that convectively forced VRWs caused acceleration of the mean wind in the lower and middle troposphere both inside and outside the eyewall and deceleration in the upper troposphere within the eyewall (Chen et al. 2003).

Hurricane Elena's (1985) rapid intensification and weakening processes were examined in reflectivity data from the Weather Surveillance Radar-1957 (WSR-57) at Apalachicola, FL (Corbosiero et al. 2005 and Corbosiero et al. 2006). The data comprised 313 radar scans of the TC's symmetric and asymmetric structure. The analysis focused on wavenumber 2 spiral bands. The outer and inner eyewall spiral

bands that propagated outward while rotating cyclonically more slowly than the mean flow were consistent with the VRW theory. The inner spiral bands emerged a few hours before the vortex experienced rapid intensification, then disappeared, and did not reappear as the storm weakened before landfall. Similarly, Romine and Wilhelmson (2006) report small scale spiral band features in a numerical simulation of Hurricane Opal (2005). They suggested that these features may have influenced hurricane intensity changes through the transport of angular momentum into the core.

In 2005, data were collected from three research aircraft flights into Hurricane Rita and Katrina during the Hurricane Rainband and Intensity Change Experiment (RAINEX, Judt and Chen 2010). Vortex Rossby waves appeared as the intense tropical cyclones experienced secondary eyewall replacement cycles. Potential vorticity changes within the hurricanes' core seem to have initiated the eyewall replacement cycles. Only Rita experienced an unambiguous eyewall replacement cycles. It was evident that the secondary PV maximum generated by convective forcing in the outer eyewall became pronounced as the eyewall contracted and the secondary wind maximum developed.

In this interpretation, wave energy was created by convection, radially transported by spiral bands, and then deposited back into the mean flow. Nonetheless, the amount of energy was often small. Furthermore, wave momentum fluxes may have weakened the vortex (e.g. Nolan et al. 2007). The result illustrated how small the effect of energy transfer from the asymmetric to symmetric flow can be. Most of the energy that allowed for vortex spin up was derived from symmetric

latent heat release. Although the vortex was somewhat affected by asymmetric processes, the dominant role of convection was forcing of the symmetric secondary flow (e.g., Schubert and Hack 1982) to intensify the primary vortex.

Qiu et al. (2010) analyzed secondary eyewall formation and Vortex Rossby waves. The simulated vortex contained inward propagating spiral rainbands and outward propagating Vortex Rossby waves. Convection in the spiral bands excited perturbations that moved PV toward the inner core of the vortex, while VRWs became elongated tangentially and compressed radially as they moved toward the outer vortex. Simultaneously, the primary eyewall shrank gradually, outer spiral bands shifted inward, and the vortex formed an intensifying secondary eyewall. The secondary eyewall ultimately became the new primary eyewall, which intensified rapidly, as a result of the VRW filamentation. According to Qiu et al. (2010), VRWs accelerate the mean flow in two ways. The first process implicated the theory projected by Montgomery and Kallenbach (1997) and the second method involved the interaction between the enhancement of convection and PV near the stagnation radius, i.e., the critical radius.

Nguyen et al. (2010) suggested that development of tropical cyclones proceeds in alternating symmetric and asymmetric episodes. They simulated Hurricane Katrina of 2005, with the high-resolution version of the Australian Bureau of Meteorology operational model for tropical-cyclone prediction (TCLAPS). The first stage is symmetric. In response to circularly symmetric heating, the mean flow developed a ring-like PV structure in the eyewall. Then, barotropic-convective instability developed leading to the formation of asymmetric Vortical Hot Towers (VHTs). For

that reason, VHT's may be interpreted as VRWs forced by asymmetric convection. The VHTs role was to redistribute potential vorticity and equivalent potential temperature as the vortex transitioned from a symmetric to an asymmetric state and the central pressure fell coincident with some weakening of the maximum wind. The wave momentum transports removed the eyewall PV maximum, setting the stage for renewed symmetric intensification.

GENERAL STRUCTURE AND PROPAGATION

While the symmetric response to heating is the dominant factor of TC intensity change, asymmetric motion that results from interaction with shearing environmental flows or internal dynamics, including VRWs, may also be important (Willoughby et al. 2007). Asymmetric convection can excite Rossby waves that affect vortex development through eddy fluxes of angular momentum. The vorticity structure near the eyewall may generate disturbances that lead to the development of the Rossby waves. For example, a reversal of the vorticity gradient inside the RMW satisfies the necessary condition for barotropic instability (Kossin et al. 2000).

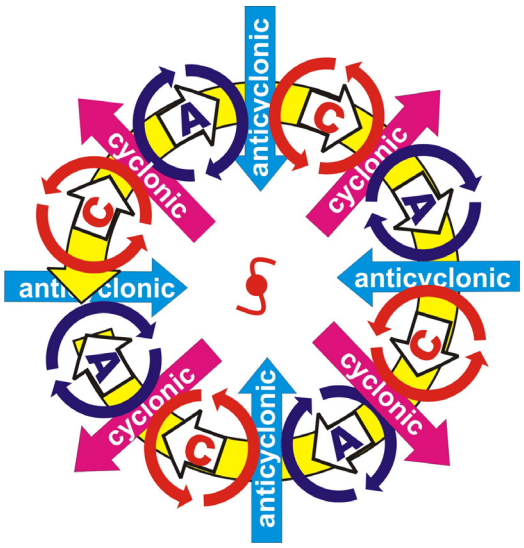

Figure 2: Simulation of Cyclonic and Anticyclonic Vortices in Tropical Cyclones.

In this study we examine nondivergent VRWs forced by imposed vorticity sources and sinks that model the effect of convection in the eyewall. Vortex Rossby Waves' phase and group velocities can be directed either outward or inward (Montgomery et al. 1995), but, as shown above, their tangential phase velocity is always directed upstream in a vortex with outwardly decreasing mean vorticity. The

waves propagate because upstream of the cyclonic eddies, outflow advects mean cyclonic vorticity outward from the vortex core, and upstream of the anticyclonic eddies inflow advects anticyclonic mean vorticity inward from the periphery. As a result, the wavetrain propagates upstream relative to the mean-flow (Figure 2).

Although VRWs propagate upstream, their group and phase velocities are relatively slow (<10 ms^{-1}) in comparison to the (~20-50 ms^{-1}) mean-flow wind. Thus, they are advected around the vortex as a train (hereafter, wavetrain) of cyclonic and anticyclonic vortices that move downstream with somewhat less than the mean-flow speed. The simplest physical system that embodies VRWs' rotational dynamics is a barotropic non-divergent model, as described in the next section.

DYNAMICS OF THE VRW BAROTROPIC NON-DIVERGENT MODEL

VORTICITY

The analysis begins with the linearized momentum equations in cylindrical coordinates (Figure 3). The variables used are $V_0(r)$, the mean tangential wind; r, radius; λ, azimuth angle (reckoned cyclonically from north); u, radial perturbation wind component; v, tangential perturbation wind component; ϕ, perturbation geopotential; and f_0, Coriolis parameter.

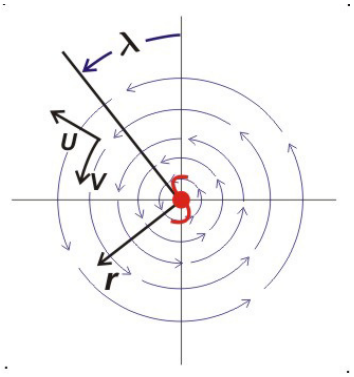

Figure 3: Cylindrical coordinate diagram.

In equations (1.1) and (1.2), $\frac{\partial}{\partial t}+\frac{V_0}{r}\frac{\partial}{\partial \lambda}$ represents the linearized individual (Lagrangian) derivatives; $\xi_0=\frac{2V_0}{r}+f_0$ is the inertial parameter; $\zeta_0=\frac{\partial V_0}{\partial r}+\frac{V_0}{r}+f$ is the mean-flow vorticity; and F_r and F_λ are the imposed forcing derived from a vector forcing potential, A, such that $F_r=\frac{1}{r}\frac{\partial A}{\partial \lambda}$ and $F_\lambda=\frac{\partial A}{\partial r}$. The formulation means that the forcing affects only the rotational part of perturbations, and not the divergent part. As shown in Figure 3, u is positive outward, v is positive cyclonically.

The linearized momentum equations are:

$$\frac{\partial u}{\partial t}+\frac{V_0}{r}\frac{\partial u}{\partial \lambda}-\left(\frac{2V_0}{r}+f_0\right)v+\frac{\partial \phi}{\partial r}=F_r \tag{1.1},$$

$$\frac{\partial v}{\partial t}+\frac{V_0}{r}\frac{\partial v}{\partial \lambda}+\left(\frac{\partial V_0}{\partial r}+\frac{V_0}{r}+f_0\right)u+\frac{1}{r}\frac{\partial \phi}{\partial \lambda}=F_\lambda \tag{1.2},$$

$$\frac{\partial u}{\partial r}+\frac{u}{r}+\frac{1}{r}\frac{\partial v}{\partial t}=0 \tag{1.3}.$$

We form a vorticity equation by taking $\frac{1}{r}\frac{\partial}{\partial \lambda}$ of (1.1) and $\frac{\partial}{\partial r}+\frac{1}{r}$ of (1.2) and simplifying,

$$\left(\frac{\partial}{\partial t}+\frac{V_0}{r}\frac{\partial}{\partial \lambda}\right)\frac{1}{r}\frac{\partial u}{\partial \lambda}-\frac{\xi_0}{r}\frac{\partial v}{\partial \lambda}+\frac{1}{r}\frac{\partial^2 \phi}{\partial r \partial \lambda}=\frac{1}{r}\frac{\partial}{\partial \lambda}F_r \tag{2.1},$$

$$\begin{aligned}&\left(\frac{\partial}{\partial t}+\frac{V_0}{r}\frac{\partial}{\partial \lambda}\right)\left(\frac{\partial v}{\partial r}+\frac{v}{r}\right)-\frac{1}{r}\frac{\partial v}{\partial \lambda}\left(\frac{\partial V_0}{\partial r}-\frac{V_0}{r}\right)+\zeta_0\left(\frac{\partial u}{\partial r}+\frac{u}{r}\right)+u\frac{\partial \zeta_0}{\partial r}+\frac{1}{r}\frac{\partial^2 \phi}{\partial r \partial \lambda}\\&=\left(\frac{\partial}{\partial r}+\frac{1}{r}\right)F_\lambda\end{aligned} \tag{2.2}.$$

We eliminate the geopotential terms by subtracting equation (2.1) from (2.3) and simplifying:

$$\begin{aligned}&\left(\frac{\partial}{\partial t}+\frac{V_0}{r}\frac{\partial}{\partial \lambda}\right)\left(\frac{\partial v}{\partial r}+\frac{v}{r}-\frac{1}{r}\frac{\partial u}{\partial \lambda}\right)-\frac{1}{r}\frac{\partial v}{\partial \lambda}\left(\frac{\partial V_0}{\partial r}-\frac{V_0}{r}\right)+\frac{\xi_0}{r}\frac{\partial v}{\partial \lambda}\\&+\zeta_0\left(\frac{\partial u}{\partial r}+\frac{u}{r}\right)+u\frac{\partial \zeta_0}{\partial r}=\left(\frac{\partial}{\partial r}+\frac{1}{r}\right)F_\lambda-\left(\frac{1}{r}\frac{\partial}{\partial \lambda}\right)F_r\end{aligned} \tag{3}.$$

The first term on the left is the Lagrangian derivative of the perturbation vorticity. To simplify, represent the difference between the vorticity and the inertial parameter as, $\zeta_0 - \xi_0 = \left(\frac{\partial V_0}{\partial r} + \frac{V_0}{r} + f_0\right) - \left(\frac{2V_0}{r} + f_0\right) = \left(\frac{\partial V_0}{\partial r} - \frac{V_0}{r}\right)$. So that,

$$\left(\frac{\partial}{\partial t} + \frac{V_0}{r}\frac{\partial}{\partial \lambda}\right)\left(\frac{\partial v}{\partial r} + \frac{v}{r} - \frac{1}{r}\frac{\partial u}{\partial \lambda}\right) + \zeta_0\left(\frac{\partial u}{\partial r} + \frac{u}{r} - \frac{1}{r}\frac{\partial v}{\partial \lambda}\right) + u\frac{\partial \zeta_0}{\partial r} = \left(\frac{\partial}{\partial r} + \frac{1}{r}\right)F_\lambda - \left(\frac{1}{r}\frac{\partial}{\partial \lambda}\right)F_r \quad (4).$$

Because the model is non-divergent we can eliminate the vorticity stretching term, $\zeta_0\left(\frac{\partial u}{\partial r} + \frac{u}{r} - \frac{1}{r}\frac{\partial v}{\partial \lambda}\right)$, thus,

$$\left(\frac{\partial}{\partial t} + \frac{V_0}{r}\frac{\partial}{\partial \lambda}\right)\left(\frac{\partial v}{\partial r} + \frac{v}{r} - \frac{1}{r}\frac{\partial u}{\partial \lambda}\right) + u\frac{\partial \zeta_0}{\partial r} = \left(\frac{\partial}{\partial r} + \frac{1}{r}\right)F_\lambda - \left(\frac{1}{r}\frac{\partial}{\partial \lambda}\right)F_r = Q \quad (5).$$

STREAMFUNCTION

Given that the flow is strictly nondivergent, it can be represented using a streamfunction ψ, such that $u = -\frac{1}{r}\frac{\partial \psi}{\partial \lambda}$ and $v = \frac{\partial \psi}{\partial r}$. Equation (5) becomes:

$$\left(\frac{\partial}{\partial t} + \frac{V_0}{r}\frac{\partial}{\partial \lambda}\right)\left(\frac{\partial^2 \psi}{\partial r^2} + \frac{1}{r}\frac{\partial \psi}{\partial r} + \frac{1}{r^2}\frac{\partial^2 \psi}{\partial \lambda^2}\right) - \frac{1}{r}\frac{\partial \psi}{\partial \lambda}\frac{\partial \zeta_0}{\partial r} = Q \quad (6).$$

VORTICITY WAVE SOLUTION

Sinusoidal wave solutions with tangential wavenumber n and frequency ω are represented in terms of the complex exponentials and a radial structure function $\psi(r,t,\lambda) = \Psi(r)e^{i(\omega t - n\lambda)}$, where Ψ is a function of r alone. The unforced left side of equation (6) simplifies to obtain the dispersion relation for free waves.

$$\left(\omega - \frac{nV_0}{r}\right)\left(\frac{d^2\Psi}{dr^2} + \frac{1}{r}\frac{d\Psi}{dr} + \frac{1}{r^2}\frac{d^2\Psi}{d\lambda^2}\right) - \left(\frac{n}{r}\frac{\partial\zeta_0}{\partial r}\right)\Psi = 0 \qquad (7),$$

Which may be solved for the Doppler shifted frequency Ω and rearranged to get the apparent frequency with respect to the ground.

$$\Omega = \left(\omega - \frac{nV_0}{r}\right) = -\frac{\left(\frac{n}{r}\frac{\partial\zeta_0}{\partial r}\right)\Psi}{\left(\frac{d^2\Psi}{dr^2} + \frac{1}{r}\frac{d\Psi}{dr} + \frac{1}{r^2}\frac{d^2\Psi}{d\lambda^2}\right)}, \text{ or} \qquad (8),$$

$$\omega = \frac{nV_0}{r} - \frac{\left(\frac{n}{r}\frac{\partial\zeta_0}{\partial r}\right)\Psi}{\left(\frac{d^2\Psi}{dr^2} + \frac{1}{r}\frac{d\Psi}{dr} + \frac{1}{r^2}\frac{d^2\Psi}{d\lambda^2}\right)} \qquad (9).$$

By assuming a convenient functional form for $\Psi(r)$, we can then solve for the apparent frequency ω (10) with respect to the ground and the Doppler shifted frequency Ω (11). Writing Ψ in terms of zero order Hankel functions $\Psi = H_0(k_r r)$, where k_r represents the radial wavenumber, yields a locally valid dispersion

relation. It is not universally valid because $\partial\zeta_0/\partial r$ and V_0 are functions of r so that k_r must be a slowly varying function of radius.

$$\omega = \frac{nV_0}{r} - \frac{\left(\frac{n}{r}\frac{\partial\zeta_0}{\partial r}\right)}{k_r\left(k_r^{\,2} + \frac{n^2}{r^2}\right)} \tag{10},$$

$$\Omega = \left(\omega - \frac{nV_0}{r}\right) = -\frac{\left(\frac{n}{r}\frac{\partial\zeta_0}{\partial r}\right)}{\left(k_r^{\,2} + \frac{n^2}{r^2}\right)} \tag{11}.$$

The radial group velocity and phase velocities respectively are:

$$C_r = \frac{\omega}{k_r} = \frac{nV_0}{k_r r} - \frac{\left(\frac{n}{r}\frac{\partial\zeta_0}{\partial r}\right)}{\left(k_r^{\,2} r + \frac{n^2}{r^2}\right)} \tag{12},$$

$$C_{gr} = \frac{\partial\omega}{\partial k_r} = \frac{2k_r\left(\frac{n}{r}\frac{\partial\zeta_0}{\partial r}\right)\left(k_r^{\,2} r + \frac{n^2}{r^2}\right)}{\left(k_r^{\,2} r + \frac{n^2}{r^2}\right)^2} \tag{13}.$$

Since the Doppler shifted frequency is always < 0, when $k_r > 0$, $C_r < 0$ (inward) and $C_{gr} > 0$; when $k_r < 0$, $C_r > 0$ (outward) and $C_{gr} < 0$, consistent with Figure 4.

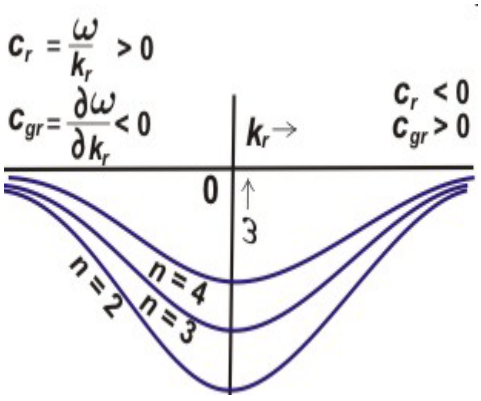

Figure 4: Rossby Wave Dispersion Relation.

LINDZEN-KUO SOLUTION

Here, we obtain linear solutions with the Lindzen and Kuo (1969) for second-order partial differential equations with boundary conditions imposed at both ends of the domain. The algorithm solves the second-order ordinary differential equation for $\Psi(r)$ subject to boundary conditions at both ends of the radial domain. Since the boundary points at the vortex center and $r = 4000$ km lie far outside the waveguide, $\Psi = 0$ is appropriate.

The differential equation $\frac{d^2\Psi}{dr^2} + g(r)\frac{d\Psi}{dr} + h(r)\Psi = Q$ can be written in finite difference form as,

$$\frac{\Psi_{n+1} + \Psi_{n-1} - 2\Psi_n}{(\delta r)^2} + g\frac{\Psi_{n+1} - \Psi_{n-1}}{2\delta r} + h\Psi_n = Q \qquad (14).$$

$$\left[\frac{1}{(\delta r)^2}-\frac{g}{2\delta r}\right]\Psi_{n-1}+\left[-\frac{2}{(\delta r)^2}+h\right]\Psi_n+\left[\frac{1}{(\delta r)^2}+\frac{g}{2\delta r}\right]\Psi_{n+1}=Q \qquad (15).$$

If, $A_n=\frac{1}{(\delta r)^2}-\frac{g(r_n)}{2\delta r}$, $B_n=-\frac{2}{(\delta r)^2}+h(r_n)$, and $C_n=\frac{1}{(\delta r)^2}+\frac{g(r_n)}{2\delta r}$ the radial structure equation in finite difference form becomes,

$$A_n\psi_{n-1}+B_n\psi_n+C_n\psi_{n+1}=Q \qquad (16).$$

The solution for equation (16) is:

$$\Psi_n=\alpha_n\Psi_{n+1}+\beta_n, \text{ or, } \Psi_{n-1}=\alpha_{n-1}\Psi_n+\beta_{n-1} \text{ for } n=1,2,3,...N \qquad (17).$$

Substitution into equation (16) produces:

$$\begin{aligned}&A_n\left[\alpha_{n-1}\Psi_n+\beta_{n-1}\right]+B_n\Psi_n+C_n\Psi_{n+1}\\&\left[A_n\alpha_{n-1}+B_n\right]\Psi_n+A_n\beta_{n-1}+C_n\psi_{n+1}=Q_n\end{aligned} \qquad (18),$$

$$\Psi_n=\frac{-C_n}{\left[A_n\alpha_{n-1}+B_n\right]}\Psi_{n+1}+\frac{\left[Q_n-A_n\beta_{n-1}\right]}{\left[A_n\alpha_{n-1}+B_n\right]} \qquad (19),$$

such that, $\alpha_n=-C_n\left[A_n\alpha_{n-1}+B_n\right]^{-1}$ and $\beta_n=\left[Q-A_n\beta_{n-1}\right]\left[A_n\alpha_{n-1}+B_n\right]^{-1}$ (20).

Since both the inner and outer boundaries lie outside the waveguides and $\Psi_1=0$, $\Psi_N=0$, then $\alpha_1=0$, $\beta_1=0$. The arrays of $\alpha_1,\alpha_2,...\alpha_{N-1}$ and $\beta_1,\beta_2,...\beta_N$ are computed using (20) in an outward pass from $n=0...N$, and then (16) is applied on an inward pass to compute $\Psi_{N-1},\Psi_{N-2},...\Psi_1$.

GEOPOTENTIAL

Once we know $\Psi(r)$, it is possible to calculate the geopotential from the divergence equation. The derivation is analogous to the vorticity equation, but with reversed order of differentiation. Take $\frac{\partial}{\partial r}+\frac{1}{r}$ of (1.1) and $\frac{1}{r}\frac{\partial}{\partial\lambda}$ of (1.2).

$$\left(\frac{\partial}{\partial t}+\frac{V_0}{r}\frac{\partial}{\partial\lambda}\right)\left(\frac{\partial u}{\partial r}+\frac{u}{r}\right)+\frac{\partial}{\partial r}\left(\frac{V_0}{r}\right)\frac{\partial u}{\partial\lambda}-\frac{\partial\xi_0}{\partial r}v-\xi_0\left(\frac{\partial v}{\partial r}+\frac{v}{r}\right)$$
$$+\frac{\partial^2\phi}{\partial r^2}+\frac{1}{r}\frac{\partial\phi}{\partial r}=\frac{\partial F_r}{\partial r}+\frac{F_r}{r} \qquad (21.1),$$

$$\left(\frac{\partial}{\partial t}+\frac{V_0}{r}\frac{\partial}{\partial\lambda}\right)\frac{1}{r}\frac{\partial v}{\partial\lambda}+\zeta_0\frac{1}{r}\frac{\partial u}{\partial\lambda}+\frac{1}{r^2}\frac{\partial^2\phi}{\partial\lambda^2}=\frac{1}{r}\frac{\partial F_\lambda}{\partial\lambda} \qquad (21.2).$$

Here, the radial gradient of the inertia parameter $\frac{\partial\xi_0}{\partial r}$ can be written as $\frac{\partial}{\partial r}\left(\frac{2V_0}{r}+f_0\right)=2\frac{\partial}{\partial r}\left(\frac{V_0}{r}\right)$. Adding (21.1, 21.2), collecting similar terms, substituting and, simplifying yields:

$$\left(\frac{\partial}{\partial t}+\frac{V_0}{r}\frac{\partial}{\partial\lambda}\right)\left(\frac{\partial u}{\partial r}+\frac{u}{r}+\frac{1}{r}\frac{\partial v}{\partial\lambda}\right)+\frac{\partial}{\partial r}\left(\frac{V_0}{r}\right)\frac{\partial u}{\partial\lambda}-2\frac{\partial}{\partial r}\left(\frac{V_0}{r}\right)v$$
$$-\xi_0\left(\frac{\partial v}{\partial r}+\frac{v}{r}\right)+\zeta_0\frac{1}{r}\frac{\partial u}{\partial\lambda}+\left(\frac{\partial^2\phi}{\partial r^2}+\frac{1}{r}\frac{\partial\phi}{\partial r}+\frac{1}{r^2}\frac{\partial^2\phi}{\partial\lambda^2}\right)=\left(\frac{\partial F_r}{\partial r}+\frac{F_r}{r}+\frac{1}{r}\frac{\partial F_\lambda}{\partial\lambda}\right) \qquad (22).$$

Adding and subtracting $-\xi_0\left(\frac{1}{r}\frac{\partial u}{\partial\lambda}\right)$, and recalling that $\frac{1}{r}(\zeta_0-\xi_0)=\frac{\partial}{\partial r}\left(\frac{V_0}{r}\right)$,

$$\left(\frac{\partial}{\partial t}+\frac{V_0}{r}\frac{\partial}{\partial \lambda}\right)\left(\frac{\partial u}{\partial r}+\frac{u}{r}+\frac{1}{r}\frac{\partial v}{\partial \lambda}\right)+\frac{2}{r}(\zeta_0-\xi_0)\left(\frac{\partial u}{\partial \lambda}-v\right)-\xi_0\left(\frac{\partial v}{\partial r}+\frac{v}{r}-\frac{1}{r}\frac{\partial u}{\partial \lambda}\right)$$
$$+\left(\frac{\partial^2\phi}{\partial r^2}+\frac{1}{r}\frac{\partial\phi}{\partial r}+\frac{1}{r^2}\frac{\partial^2\phi}{\partial\lambda^2}\right)=\left(\frac{\partial F_r}{\partial r}+\frac{F_r}{r}+\frac{1}{r}\frac{\partial F_\lambda}{\partial\lambda}\right) \qquad (23).$$

Since the flow is rotational and the forcing is derived from a vector potential, $\nabla\cdot v=0$ and $\nabla\cdot F=0$. We rearrange the remaining terms to get a Poisson equation for the geopotential:

$$\left(\frac{\partial^2\phi}{\partial r^2}+\frac{1}{r}\frac{\partial\phi}{\partial r}+\frac{1}{r^2}\frac{\partial^2\phi}{\partial\lambda^2}\right)=-\frac{2}{r}(\zeta_0-\xi_0)\left(\frac{\partial u}{\partial\lambda}-v\right)+\xi_0\left(\frac{\partial v}{\partial r}+\frac{v}{r}-\frac{1}{r}\frac{\partial u}{\partial\lambda}\right) \qquad (24),$$

or,

$$\left(\frac{\partial^2\phi}{\partial r^2}+\frac{1}{r}\frac{\partial\phi}{\partial r}+\frac{1}{r^2}\frac{\partial^2\phi}{\partial\lambda^2}\right)=-\frac{2}{r}(\zeta_0-\xi_0)\left(-\frac{1}{r}\frac{\partial^2\psi}{\partial\lambda^2}-\frac{\partial\psi}{\partial r}\right)$$
$$+\xi_0\left(\frac{\partial^2\psi}{\partial r^2}+\frac{1}{r}\frac{\partial\psi}{\partial r}+\frac{1}{r^2}\frac{\partial^2\psi}{\partial\lambda^2}\right) \qquad (25).$$

By analogy with the streamfunction, the solution for the geopotential takes the form $\phi=\Phi(r)e^{-i(\omega t-n\lambda)}$,

$$\left(\frac{d^2\Phi}{dr^2}+\frac{1}{r}\frac{d\Phi}{dr}-\frac{n^2\Phi}{r^2}\right)=-\frac{2}{r}(\zeta_0-\xi_0)\left(\frac{n^2}{r}\Psi-\frac{d\Psi}{dr}\right)$$
$$+\xi_0\left(\frac{d^2\Psi}{dr^2}+\frac{1}{r}\frac{d\Psi}{dr}-\frac{n^2}{r^2}\Psi\right) \qquad (26),$$

which can be solved for ϕ with the Lindzen-Kuo algorithm, as above.

ELIASSEN PALM RELATION

The Eliassen Palm relation provides insight into eddy wave energy and angular momentum fluxes as well as wave-mean-flow interactions (Painemal 2004). It is an excellent tool for better understanding of eddy dynamics and propagation of energy and angular momentum. The derivation begins with the linearized tangential momentum equation:

$$\left(\frac{\partial}{\partial t}+\frac{V_0}{r}\frac{\partial}{\partial x}\right)v+u\zeta_0+\frac{1}{r}\frac{\partial\phi}{\partial\lambda}=0 \qquad (27).$$

Equation (27) can be written as $i\left(\omega-\frac{nV_0}{r}\right)v+u\zeta_0+\frac{1}{r}\frac{\partial\phi}{\partial\lambda}=0$; where, the Doppler-shifted frequency is $\Omega=\omega-\frac{nV_0}{r}$. Next, we factor out $\frac{n}{r}$ from the mean flow:

$$\frac{in}{r}\left(\frac{\omega r}{n}-V_0\right)v+u\zeta_0+\frac{1}{r}\frac{\partial\phi}{\partial\lambda}=0 \qquad (28).$$

Here, $C_0=\frac{\omega r}{n}$ so that the equation becomes $\left(C_0-V_0\right)\frac{inv}{r}+u\zeta_0+\frac{1}{r}\frac{\partial\phi}{\partial\lambda}=0$. Since, $\frac{inv}{r}\rightarrow-\frac{1}{r}\frac{\partial v}{\partial\lambda}$, the equation becomes:

$$\left(-C_0+V_0\right)\frac{1}{r}\frac{\partial v}{\partial\lambda}+u\zeta_0+\frac{1}{r}\frac{\partial\phi}{\partial\lambda}=0 \qquad (29).$$

Multiplying (29) by $\left(-C_0+V_0\right)v+\phi$ and simplifying,

$$\left(-C_0+V_0\right)^2\frac{1}{r}\frac{\partial}{\partial\lambda}\left(\frac{v^2}{2}\right)+\zeta_0\left(-C_0+V_0\right)uv+\left(-C_0+V_0\right)v\frac{1}{r}\frac{\partial\phi}{\partial\lambda}$$
$$+\left(-C_0+V_0\right)\phi\frac{1}{r}\frac{\partial v}{\partial\lambda}+\zeta_0u\phi+\frac{1}{r}\frac{\partial}{\partial\lambda}\frac{\phi^2}{2}=0 \qquad (30),$$

$$\left(-C_0+V_0\right)^2\frac{1}{r}\frac{\partial}{\partial\lambda}\left(\frac{v^2}{2}\right)+\zeta_0\left[\left(-C_0+V_0\right)uv+u\phi\right]$$
$$+\left(-C_0+V_0\right)\frac{1}{r}\frac{\partial}{\partial\lambda}v\phi+\frac{1}{r}\frac{\partial}{\partial\lambda}\frac{\phi^2}{2}=0 \qquad (31).$$

By integrating around a circle at fixed radius, $\langle()\rangle=\int_0^{2\pi}()d\lambda$, all exact $\frac{\partial}{\partial\lambda}$ derivatives integrate to zero, eliminating the vorticity terms, so that $\left(-C_0+V_0\right)\langle uv\rangle+\langle u\phi\rangle=0$. Next we multiply $\frac{n}{r}\frac{r}{n}$ and substitute for Ω:

$$-\frac{\Omega r}{n}\langle uv\rangle+\langle u\phi\rangle=0\text{, or }\ \Omega r\langle uv\rangle=n\langle u\phi\rangle \qquad (32).$$

In (32), the product of the Doppler-shifted frequency with the eddy angular momentum flux equals the eddy geopotential flux. Since for VRWs $\Omega<0$, this relation shows that outward propagating wave energy, $\langle u\phi\rangle>0$, requires that angular momentum must propagate inward, $\Omega r\langle uv\rangle<0$.

The propagation of wave-energy packets is naturally away from the source. For forcing in the eyewall, energy from the locus of the forcing propagates both inward toward the cut-off radius and outward toward the critical radius. Near the critical radius, at the outer edge of the waveguide, the group velocity is almost zero; here, the wave-energy packets stagnate and are eventually absorbed. At the inner edge of the waveguide, the frequency is Doppler shifted to the cut-off frequency, the energy

is reflected, travels outward, back across the RMW to the outer boundary of the waveguide where it, too, is absorbed near the critical radius.

The initially inward propagating energy packets support an outward angular momentum flux that is balanced by angular momentum carried by the waves reflected from the inner boundary of the waveguide where Ω equals the cut-off frequency. The initially outward propagating packets carry energy towards the critical radius and angular momentum toward the locus of forcing. Thus, there is a divergence of wave energy from the source, a convergence of wave energy around the critical radius, a divergence of angular momentum from the neighborhood of the critical radius, and a convergence of angular momentum where the waves are forced near the RMW, which in turn intensifies the strongest winds. The present wavenumber 2, barotropic, non-divergent model is the simplest one that represents the rotational dynamics of this process.

FORCING

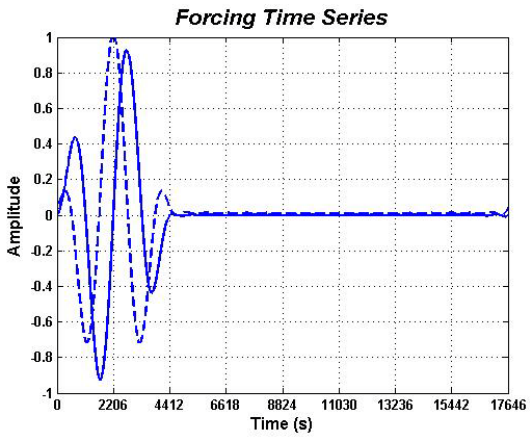

Figure 5: The forcing time series calculated from the Fourier series.

The forcing used here is cyclic with alternating active and quiescent intervals. While the forcing is active, it rotates with frequency ω that corresponds to a period of 2206 s. At the initial startup time, the forcing turns on and remains on for 4412 s, or ¼ of the total period. This is the Active time in Figure 5. The remaining ¾ of the period is quiescent. The forcing is turned off until the beginning of the next period. In this representation, the forcing rises to a maximum and subsides. Subsequently, the waves propagate and ultimately dissipate, returning to the initial startup configuration by the end of the period at 17646 s.

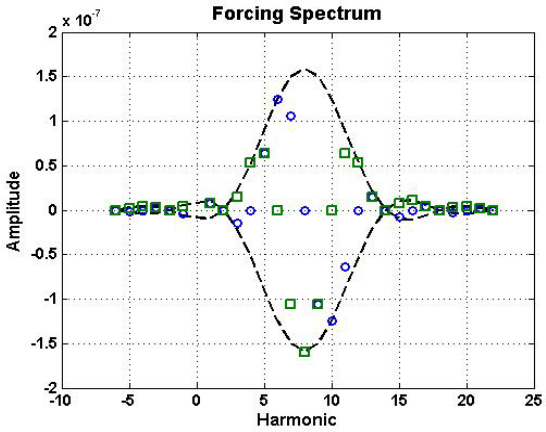

Figure 6: The forcing spectrum. The squares and circles are the real and imaginary values and the dashed lines represent the magnitude of forcing.

The forcing is represented as a superposition of sinusoidal Fourier components (e.g. Churchill 1963). The harmonics of the complex forcing interfere constructively

during the active phase and interfere destructively during the quiescent phase. Each harmonic has a constant amplitude and relative phase determined by its complex Fourier coefficient. The frequency of the n^{th} harmonic is n times the frequency of the fundamental. A spectrum of 28 harmonics is adequate to represent the forcing with minimal Gibbs phenomenon.

The forcing spectrum (Figure 6) shows the distribution of the amplitude and phase for harmonics −6 to 22. The green squares correspond to the imaginary parts; the blue circles represent real parts; and the dashed curve is the magnitude of the forcing. Peak spectral amplitude corresponds to the 8th harmonic, which is also the rotation frequency of the forcing while it is active. In this case, the frequency at the peak amplitude is 0.6 of the rotation frequency of air moving with the wind at the radius where the forcing is applied. The choice of $0.6\,V/r$ produces the widest waveguide for the 8th harmonic and is consistent with the observed rotation of eyewall convection (e.g., Black et al. 2002 and Figures A4 and A5). Only harmonics 4 through 12 contained power levels that contributed significantly to the wave energy.

FREQUENCY VARIATION AND ANGULAR MOMENTUM TRANSPORT

Vortex Rossby waves can propagate only when their Doppler shifted frequency is between the critical frequency, $\Omega = 0$, and the cut-off frequency, $\Omega = -\frac{r}{n}\frac{\partial \zeta}{\partial r}$. These frequencies define the VRW passband, and the radii where the Doppler-shifted frequencies equal the cut-off frequency and zero define an annular waveguide within which VRWs can propagate. The latter frequency is the most negative frequency

that can sustain sinusoidal vorticity waves. The radial wavenumber k_r goes to zero as the waves approach the Rossby wave cut-off frequency (Figure 7).

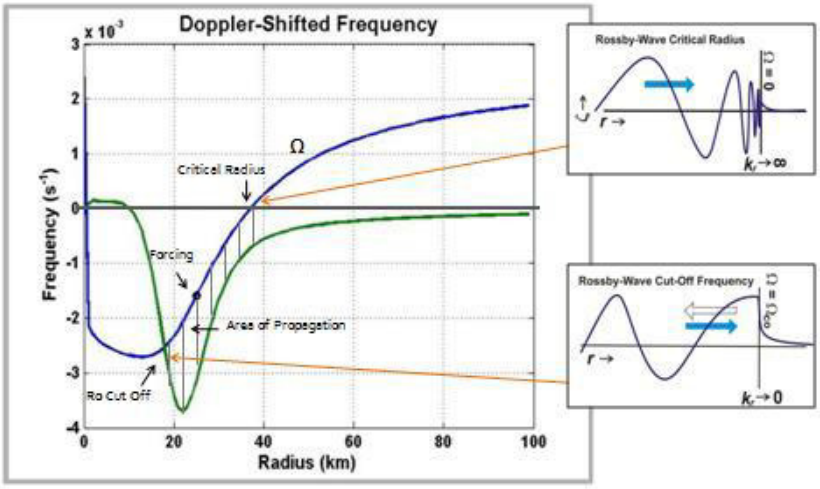

Figure 7: Wave Propagation. The left diagram displays the Doppler shifted frequencies (blue line) and the apparent frequency (green line). The forcing (black dot) is placed at $r = 25$km. The shaded area defines the waveguide where Rossby waves can propagate. The upper right diagram shows the propagation as the waves approach the Rossby wave critical radius. Here, the waves are tightly filamented and absorbed. The lower right diagram illustrates the propagation as the waves approach the Rossby Waves cut-off frequency where they are reflected.

Initially, the forcing will generate some inward propagating waves. Once these waves' frequencies reach the cut-off frequency, their tangential propagation is like one dimensional Rossby waves and their energy is reflected outward. Conversely, k_r goes to infinity as the Doppler shifted frequencies of outward propagating waves approach zero frequency at the critical radius. The wave phase lines become more tightly packed with increasing radius and the wave energy is absorbed. Some of the wave energy may leak past the critical radius if there is an outer waveguide where the waves can propagate. Nevertheless, the overall energy propagation past the critical radius is small.

WAVEGUIDES

Harmonics 4, 6, 8, 10, and 12 with tangential wavenumber 2 forcing propagate in a set of waveguides that extends from a minimum of 14 km radius for the 4th

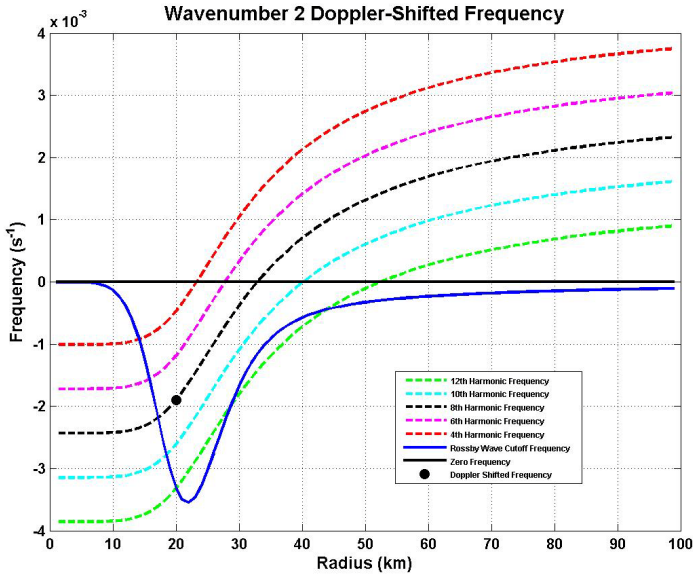

Figure 8: Wavenumber 2 Doppler Shifted Frequency of Harmonic Numbers 4, 6, 8, 10, and 12.

harmonic to a maximum of 40 km for the 10th harmonic. Locations of the cut-off and critical radius are different for each harmonic (Figure 8). The waveguide for the 8th harmonic extends from 17 km to 33 km, and the 12th harmonic has an additional outer waveguide from 44 km to 50 km. Because the fundamental frequency is multiplied by the harmonic index, the negative frequency of the 4th harmonic number is less negative than the frequency of the 12thharmonic. Therefore, the critical radius and cut-off frequency are located farther from the center for higher harmonics.

The waveguides are widest for harmonics 6, 8, and 10. These forced waves can easily transport energy between the cut-off and the critical radii. The 8th harmonic can propagate from 17 km to 35 km for a total width of about 18 km. The low frequency of the 4th harmonic moves the cut-off radius to 15 km but it also causes the critical radius to lie at 25 km. Thus, this wave can propagate in a waveguide only 10 km wide.

The solution for the 12th harmonic is different. Here, the high frequency places the cut-off frequency farther away from the center, at about 20 km. The waves quickly encounter another cut-off boundary before they reach the critical radius. Thus, the waves are potentially trapped between two cut-off radii at 20 km and 28 km radius and between yet another cut-off at 45 km and the critical radius at 50 km. The waves can "tunnel" only a small amount of energy into the outer waveguide. Consequently, the 12th harmonic presents a complicated structure and does not sustain strong radial VRW energy propagation. Since harmonics smaller than 4 have negative frequencies that are too low and harmonics larger than 12 have negative frequencies that are too high, they do not sustain propagating waves.

WAVENUMBER 2 SOLUTIONS

The wavenumber 2 phases of the forcing, streamfunction, vorticity, and geopotential span 135 degrees of azimuth relative to the 8th harmonic. The forcing is near strongest at time t = 2400 s (Figure 9) while the amplitude continues to increase through t = 3600 s (Figure 11a). The vorticity fields in this model behave much like those in previous studies (e.g., Montgomery and Kallenbach, 1997). The streamfunction and geopotential reveal VRW dynamics and the relationship among the forcing, vorticity, and wind fields. Because the vorticity is the Laplacian of the streamfunction, the streamfunction and vorticity tend to be 180 degrees out of phase. Since solving the Poisson equations for streamfunction or vorticity is a powerful smoother, streamfunction and geopotential are much less noisy fields than vorticity.

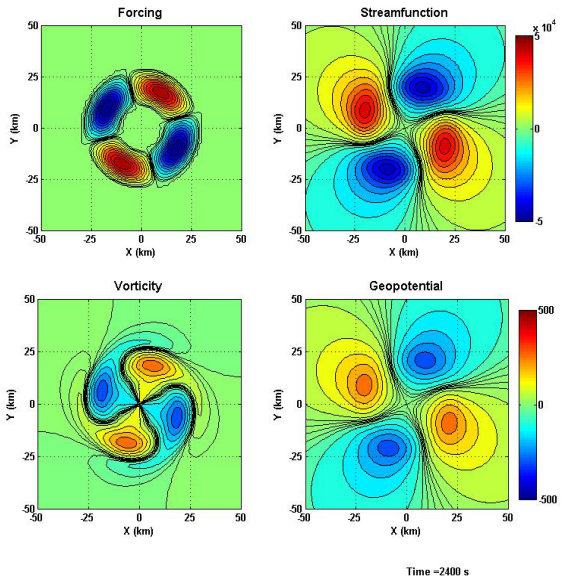

Figure 9: Complete Forcing, Streamfunction, Vorticity, and Geopotential fields at time $t =$ 2400 seconds.

The radial geopotential flux represents energy propagating with the radial group velocity of each harmonic. Moreover, the energy transports and momentum are connected through the Sawyer-Eliassen relation so that wave energy and momentum propagate in opposite directions for $\Omega < 0$. The geopotential's radial structure is similar but not identical to the streamfunction's solutions.

HARMONICS 4, 6, 8, 10, AND 12

The wavenumber 2 model yields forcing, streamfunction, vorticity, and geopotential for harmonics 4, 6, 8, 10, and 12, which are the basis for analysis of the wave properties. In Figures 10a-e, the upper four diagrams display the n^{th} harmonic radial structure and eddy fluxes as functions of radius, while the lower four diagrams are fields of the two dimensional solutions. In the upper group, the upper

left panel shows the real and imaginary parts of the streamfunction; the lower left is the real and imaginary vorticity; the upper right is the eddy momentum flux; and the lower right is the eddy geopotential flux. The blue lines in the streamfunction and vorticity plot represent the real parts of the solutions and the green lines represent the imaginary parts. In the lower group, the upper left contour plot is the forcing; the upper right is the streamfunction; the lower left is the vorticity; and the lower right is the geopotential. It is important to keep in mind that the only time variation that these components exhibit is rotation with their specified frequencies.

The 4th harmonic is weakly forced and has correspondingly small streamfunction, vorticity, and geopotential. The vorticity exhibits some filamentation near the critical radius and the streamfunction and geopotential gyres are more or less elliptical and relatively broad. The vorticity radial structure has two maxima: one near the base of the inner teardrop-shaped anomaly and the second defining the outer gyre. The maxima of the angular momentum and geopotential fluxes are more or less centered in the waveguide. As expected from the Eliassen-Palm relation for $\Omega < 0$, $\langle u\phi \rangle > 0$ and $r\langle uv \rangle < 0$.

Harmonics 6, 8, and 10 display similar results for all wave properties. In the 6th harmonic, the streamfunction gyres begins to exhibit trailing-spiral structures and lag about $\pi/2$ behind the forcing center and have opposite signs. The vorticity anomalies are stronger with sheared edges, exhibiting tail-like filaments that wrap around the center near the critical radius. The filamented anomalies are located at approximately $r = 30$ km. Although the evanescent end of the geopotential flux extends beyond the critical radius, the magnitudes of the angular momentum and

geopotential fluxes within the waveguide are stronger than those of the lower harmonic numbers.

The 8th harmonic is the most strongly forced and has the largest streamfunction and geopotential values. The streamfunction exhibits more pronounced trailing spiral structures and stronger gradients at 18-35 km radius. The 8th harmonic vorticity is filamented and tightly wound in the neighborhood of the critical radius at approximately 35 km. The radial structure of the vorticity exhibits three extrema: the first is at the inner boundary of the waveguide, and the second and third are in the region where the filamented spirals become tightly wound.

The streamfunction for 10th harmonic is weaker. Vorticity anomalies are smaller, confined within the narrower waveguide, and even more tightly wound at the critical radius.

The 12th harmonic is near the high-frequency end of the propagating part of the spectrum. The forcing is much like the forcing seen in the 4th harmonic. Even though the streamfunction and geopotential amplitudes are much smaller, the trailing spirals structure remains. The vorticity filamentation is evident at the critical radius but over a smaller radial interval.

Harmonic 4, 6, 8, 10, and 12 Wavenumber 2 Solutions

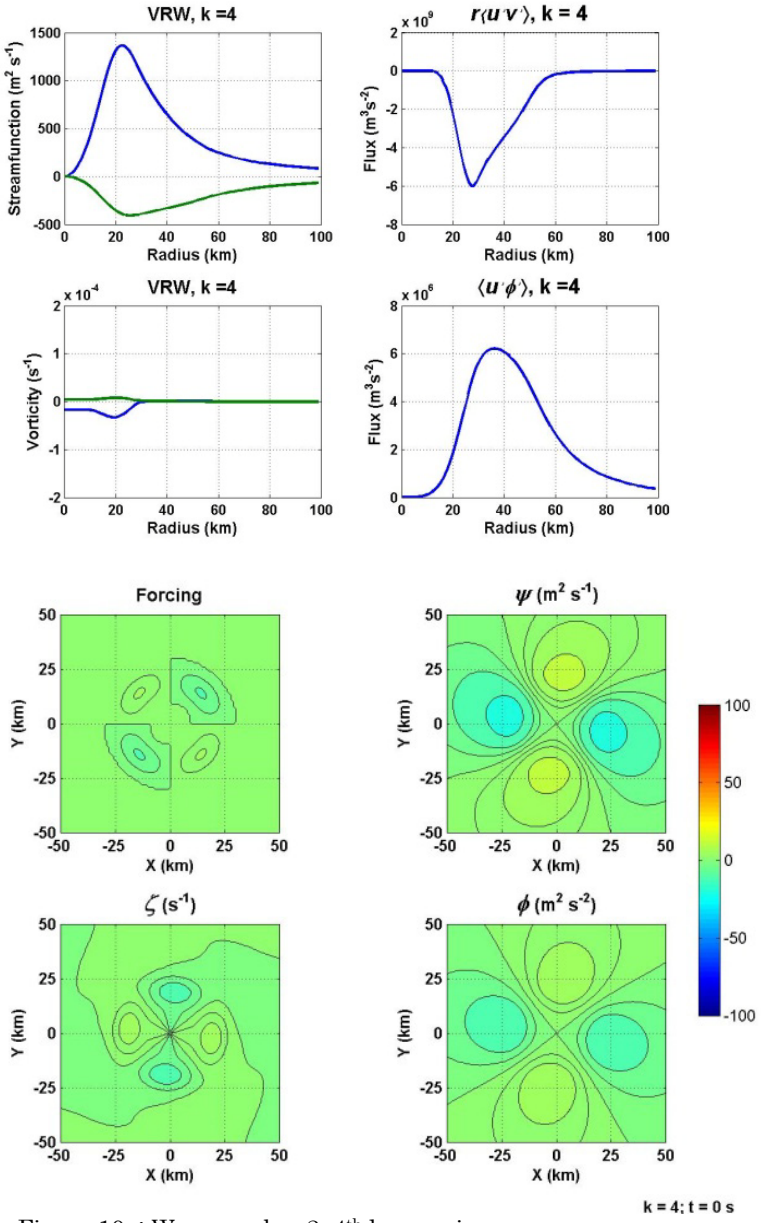

Figure 10a: Wavenumber 2, 4th harmonic.

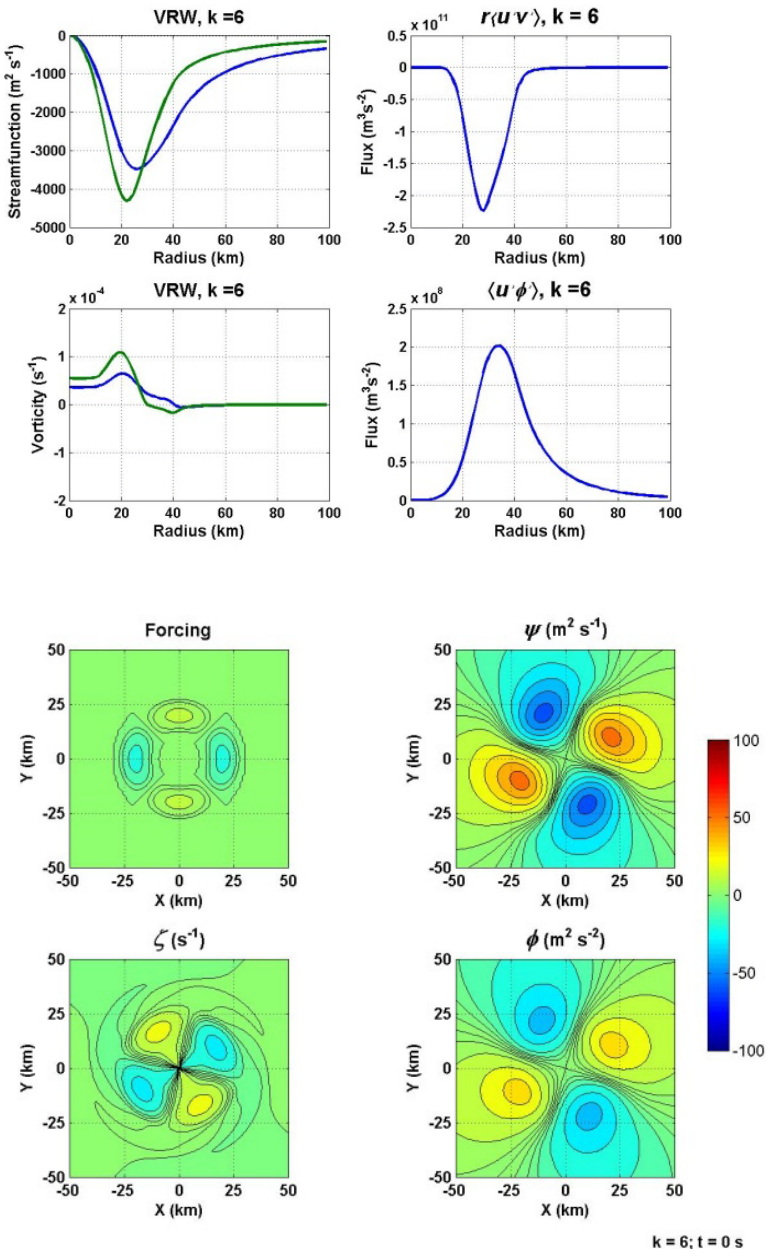

Figure 10b: Wavenumber 2, 6th harmonic.

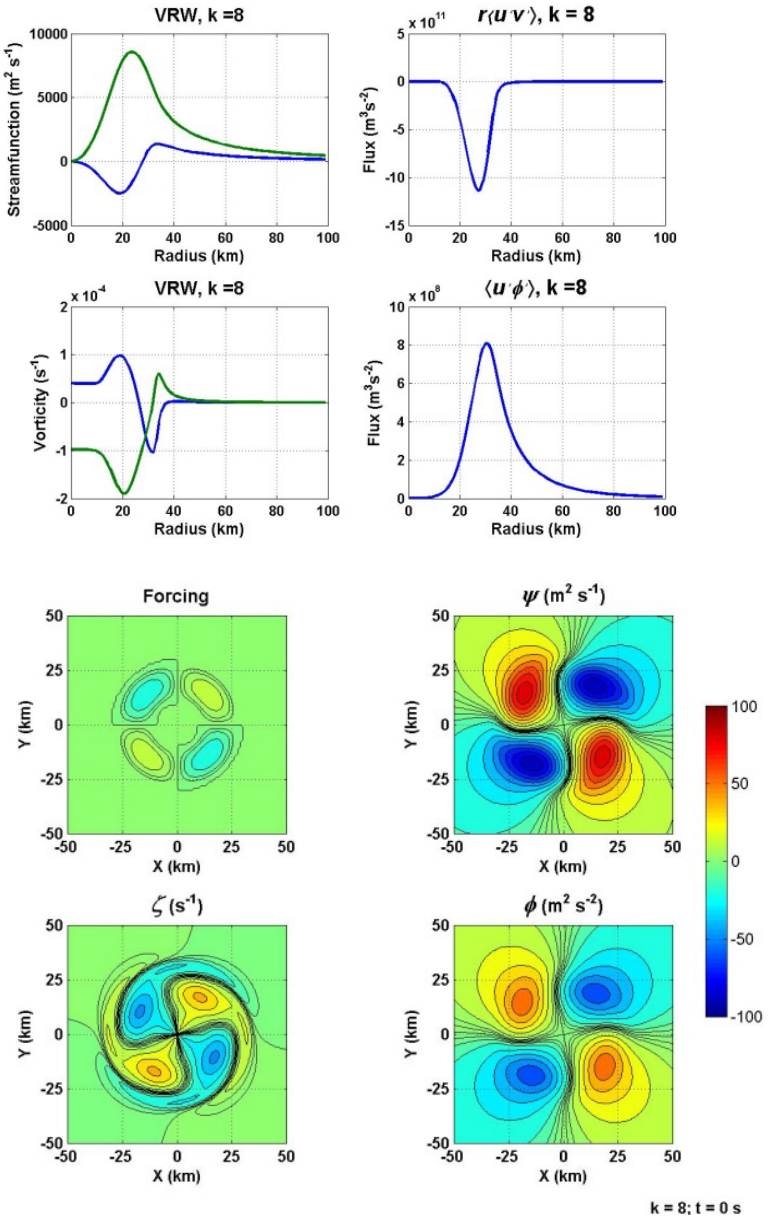

Figure 10c: Wavenumber 2, 8th harmonic.

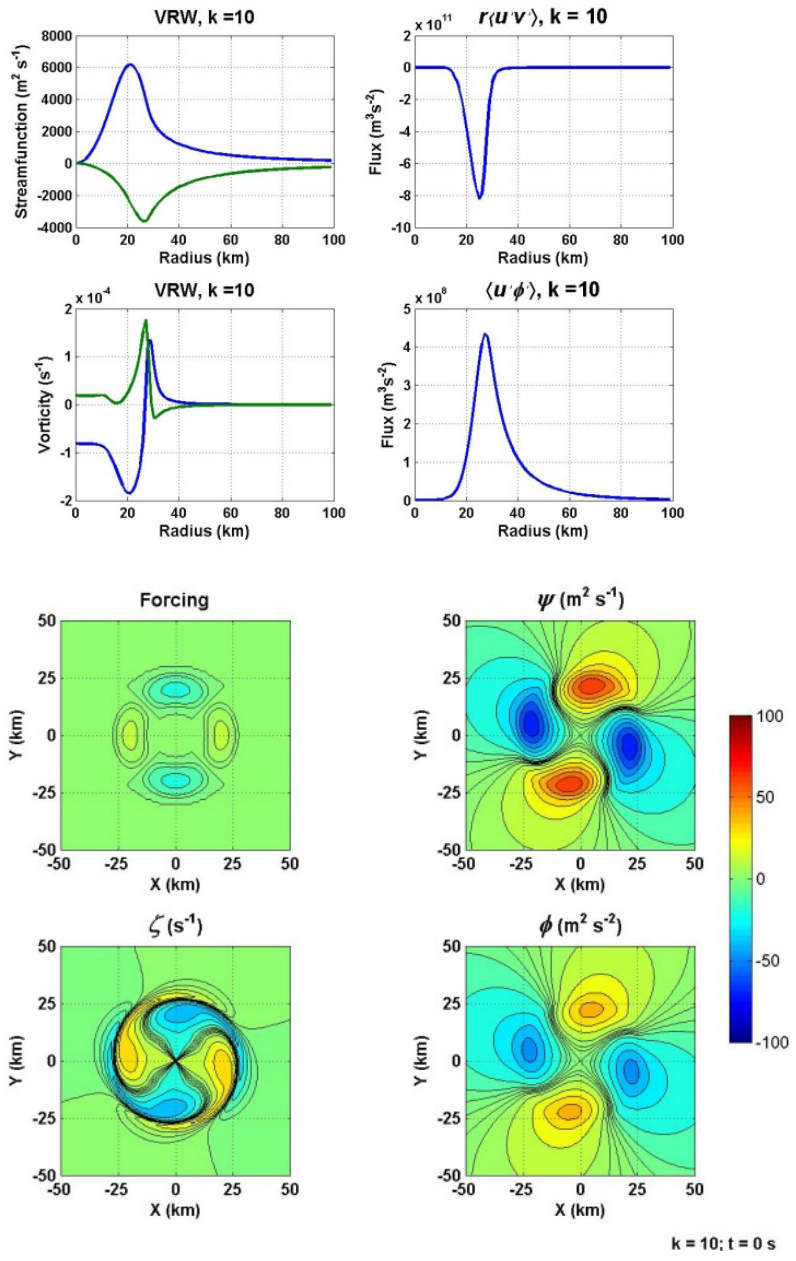

Figure 10d: Wavenumber 2, 10th harmonic.

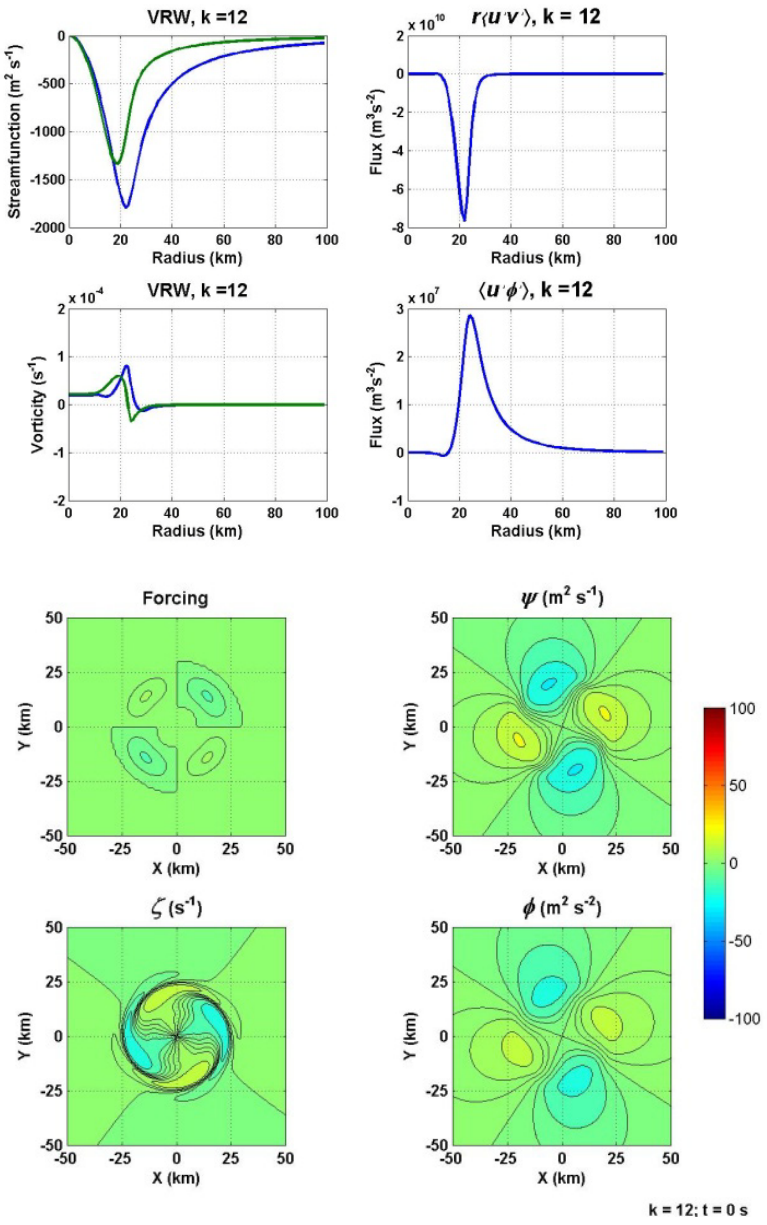

Figure 10e: Wavenumber 2, 12th harmonic.

The results for all the harmonics are comparable with Figure 8. The forcing, streamfunction, vorticity, and geopotential characteristics fall within the waveguides for harmonic numbers 4, 6, 8, 10, and 12. By design, the 8th harmonic number has the widest radial interval.

FORCING, STREAMFUNCTION, VORTICITY, AND GEOPOTENTIAL IN THE COMPLETE SOLUTION

Figure 11 displays Fourier Synthesis of the total forcing, streamfunction, vorticity, and geopotential for the complete solution at two selected times during a complete cycle of 17,646 seconds. The forcing is active at the first of these times, t = 3600 s and inactive at the second time t = 4800 s.

At time t = 3600 s, the largest amplitudes occur. Somewhat after the time peak forcing, streamfunction and geopotential trailing spirals with vorticity masking are prevalent. Cool colors represent positive (anticyclonic) streamfunction values and warm colors represent negative (cyclonic) values. The gyres rotate counterclockwise following the centers of forcing with about 180 degrees phase lag. Because the streamfunction takes on the opposite sign from vorticity, the positive forcing and negative streamfunction gyre corresponds to cyclonic circulations while the negative forcing and positive streamfunction corresponds to anticyclonic circulations. The physical structure of these trailing spirals, however, differs from those documented in previous studies (e.g., Montgomery and Kallenbach, 1997).

At 4800 s, the model clearly depicts vorticity filamentation near the critical radius. Its characteristics are much like the features seen in previous studies—sheared anomalies that wrap around the vortex and become increasingly tightly wound together near the critical radius. Late in the period (not shown here), the positive and negative vorticity filaments cancel to produce zero net local vorticity. The model's streamfunction and geopotential, however, do not behave in the same way. Even though vorticity masking persists, the gyres of both dissipate once the forcing turns off.

Wavenumber 2 Forcing, Streamfunction, Vorticity, and Geopotential

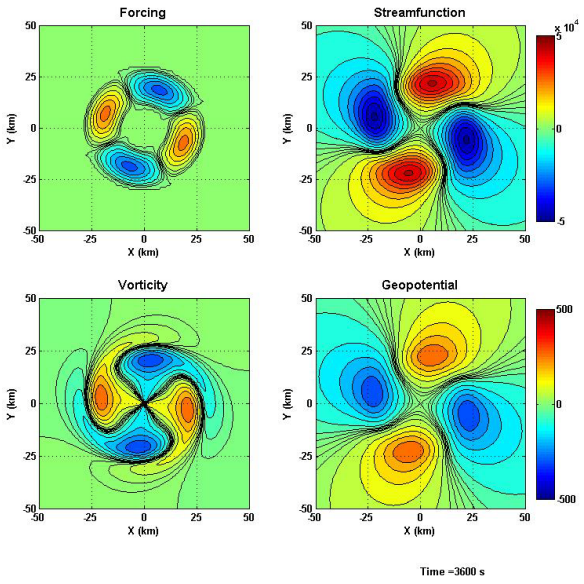

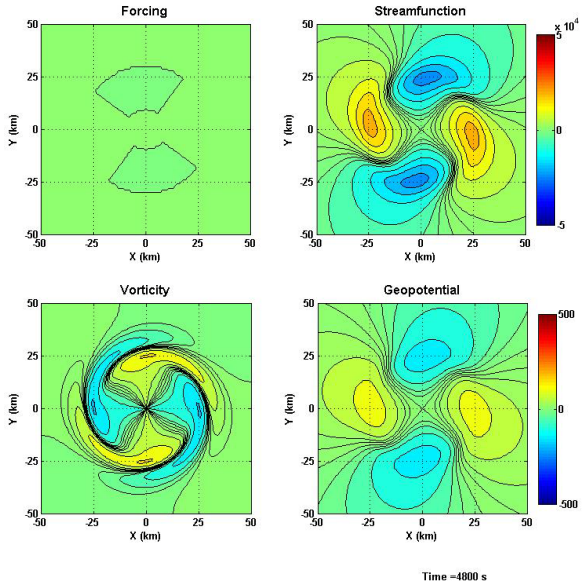

Figure 11: Wavenumber 2 solutions at times t = 3600 s and t = 4800 s.

At the earlier time, the forcing has spun up positive (cyclonic) and negative (anticyclonic) streamfunction and geopotential gyres. During the interval between snapshots, the forcing, streamfunction, vorticity, and geopotential rotated almost 180 degrees cyclonically. From time t = 0 up to time t = 4406 s (between the times illustrated), they complete two full rotations and the forcing has increased to its maximum and then decreased to zero. By the end of the first 3600 s, the model clearly depicts vorticity filamentation near the critical radius.

After the forcing subsides, represented at time t = 4800 s, the spirals weaken slowly and ultimately decay almost completely before the next cycle begins. The vorticity, however, continues to stretch and wrap around the vortex. Because the vorticity pattern becomes strongly filamented by the end of the period, the net vorticity is near zero throughout the vortex.

STREAMFUNCTION AND VORTICITY OF THE COMPLETE SOLUTION

This segment, illustrates Fourier synthesis of the complete wavenumber 2 streamfunction (Figure 12, left panels) and vorticity (Figure 12, right panels). The images represent a complete cycle at intervals of 600 seconds, as before. Initially, the forcing has just turned on and the streamfunction is essentially zero, but, the vorticity plot contains some of the residual vorticity from the previous cycle (Figure 12a). The residual is, however, small and does not significantly change the general structure of the field. The Newtonian dissipation parameter was adjusted to improve the appearance of the vorticity results by reducing the residual.

By time $t = 600$ s, the streamfunction develops elliptical gyres that line up with tear-drop shaped vorticity anomalies of opposite sign (Figure 12b). After approximately 1800 s, trailing-spiral streamfunction structure and some vorticity masking becomes evident (Figure 12d).

The vorticity and streamfunction reach maximum amplitude near 3600 seconds (Figure 12f, see also Figure 11a). The strongest streamfunction gradient is near the 8^{th} harmonic's critical radius at ~ 20-25 km. The vorticity maximum is located at approximately $r = 20$ km, nearly the same radius. In the vorticity radial structure plot (Figure 10c), the components change sign near 30 km radius. In Figure 12f, filamentation begins in the same region. Once the forcing weakens and finally stops, the streamfunction around the vortex center weakens as the wave energy propagates outward and the vorticity continues to filament more tightly near the critical radius (Figure 12i-l). Eventually, after 7200 s, the streamfunction amplitude dies away but highly filamented vorticity remains (Figures 12m-q). Near the end of

the cycle, the vorticity anomalies are very elongated and tightly wound. Thus, it implies that the net vorticity in the neighborhood of any point near the critical radius is virtually zero, so that net forcing in the Poisson solution for the streamfunction is weak, resulting in small streamfunction amplitude. As the next cycle begins, new vorticity is generated and entwined with the residual vorticity from the last cycle.

The Wavenumber 2 results illustrate the relationship between the forcing, streamfunction, geopotential, and vorticity for the complete Fourier wavetrain. The results describe the evolution of streamfunction from elliptical gyres to trailing spirals and finally to vorticity damped filaments during the course of one complete cycle.

Streamfunction and Vorticity

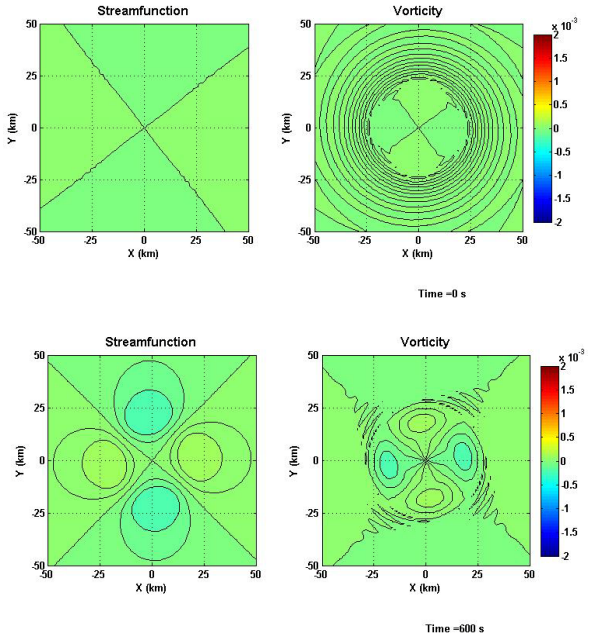

(a)

(b)

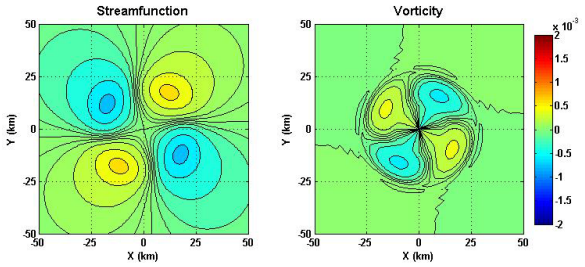
Streamfunction
Vorticity
Y (km)
X (km)
x 10^-3
Time =1200 s

(c)

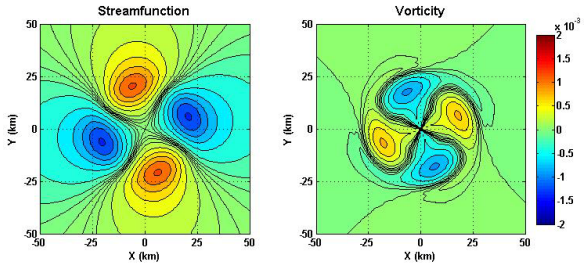
Streamfunction
Vorticity
Y (km)
X (km)
x 10^-3
Time =1800 s

(d)

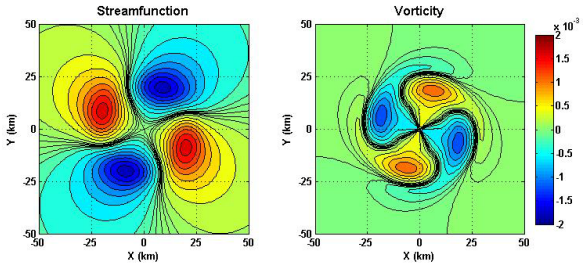
Streamfunction
Vorticity
Y (km)
X (km)
x 10^-3
Time =2400 s

(e)

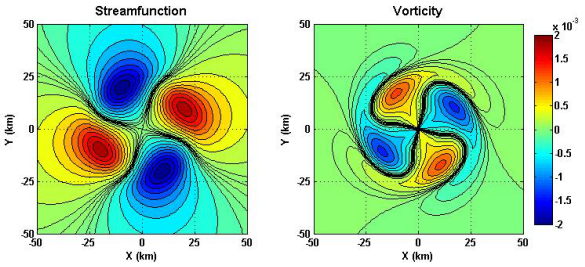
Streamfunction
Vorticity
Y (km)
X (km)
x 10^-3
Time =3000 s

(f)

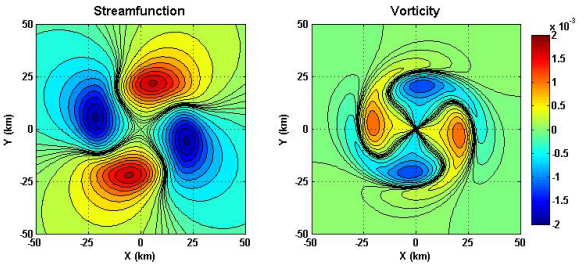
Streamfunction
Vorticity
Y (km)
X (km)
x 10^-3
Time =3600 s

(g)

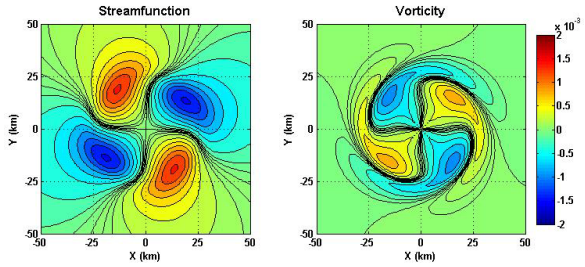
Streamfunction
Vorticity
Y (km)
X (km)
x 10^-3
Time =4200 s

(h)

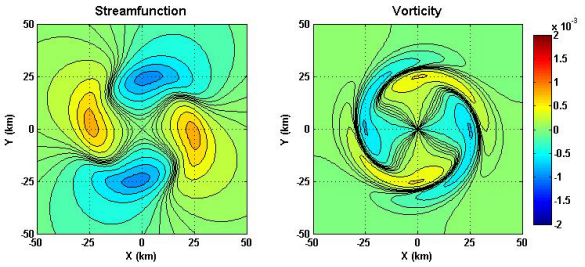
Streamfunction
Vorticity
Y (km)
X (km)
x 10^-3
Time =4800 s

(i)

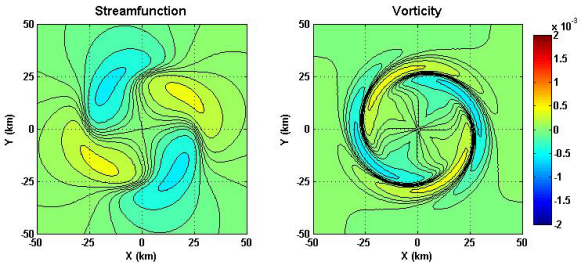
Streamfunction
Vorticity
Y (km)
X (km)
x 10^-3
Time =5400 s

(j)

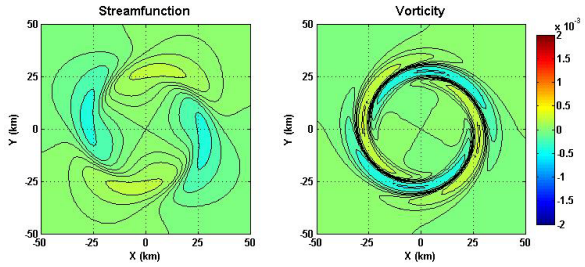
Streamfunction
Vorticity
Y (km)
X (km)
x 10^-3
Time =6000 s

(k)

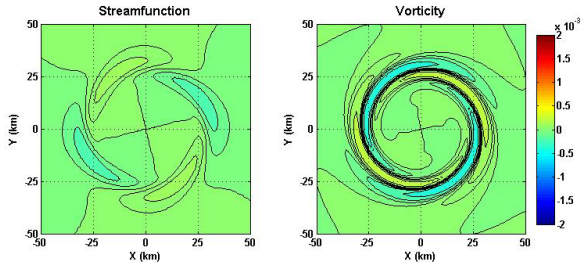
Streamfunction
Vorticity
Y (km)
X (km)
x 10^-3
Time =6600 s

(l)

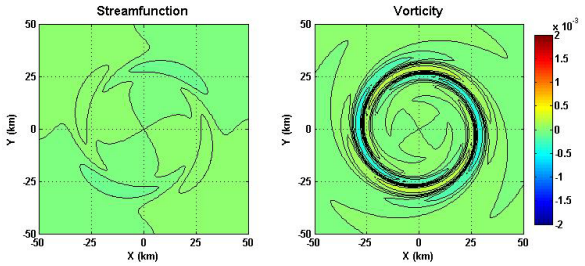
Streamfunction
Vorticity
Y (km)
X (km)
x 10^-3
Time =7200 s

(m)

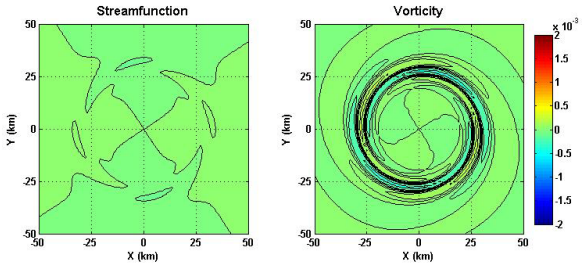
Streamfunction
Vorticity
Y (km)
X (km)
x 10^-3
Time =7800 s

(n)

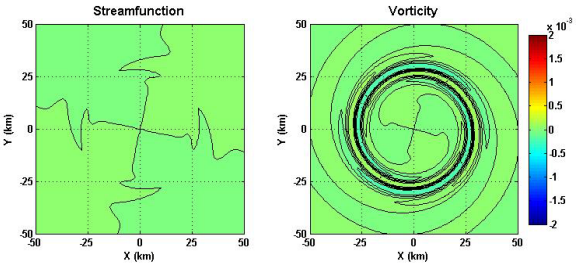
Streamfunction
Vorticity
Y (km)
X (km)
x 10^-3
Time =8400 s

(o)

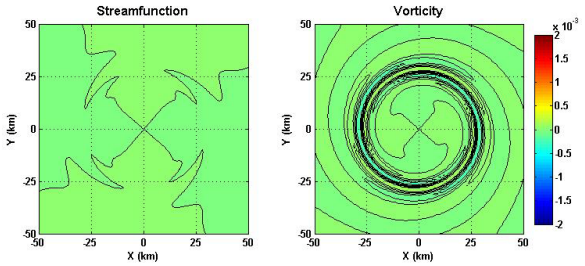
Streamfunction
Vorticity
Y (km)
X (km)
x 10^-3
Time =9000 s

(p)

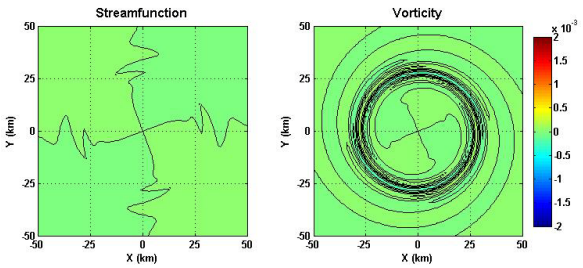

(q)

Time =9600 s

Figure 12a-q: The streamfunction (left) and vorticity (right) for a complete solution in 600 second intervals.

WAVENUMBER 3 AND WAVENUMBER 4 FORCING IN THE COMPLETE SOLUTION

The wavenumbers 3 and 4 are modeled to evaluate the representativeness of wavenumber 2. In order to obtain the widest possible waveguide for the wavenumber 3 solution, the frequency at peak amplitude was increased to 0.85. As a result, only harmonic number 6, 8, and 10 fall within the Rossby-wave passband (Figure 13). The numbers of streamfunction and geopotential gyres, as well as the vorticity anomalies, increase and are confined to a radially narrower waveguide.

As before, the solutions for (Figures 14a-e) harmonics 6 and 8 exhibit trailing streamfunction spirals and vorticity filamentation near the critical radius. Although within the VRW propagation range, the 10^{th} harmonic is weakly forced and exhibits streamfunction spirals with distorted vorticity structure. To provide a more complete overview, the forcing, streamfunction, vorticity, and geopotential of the complete wavenumber 3 solution appear in Figure 15.

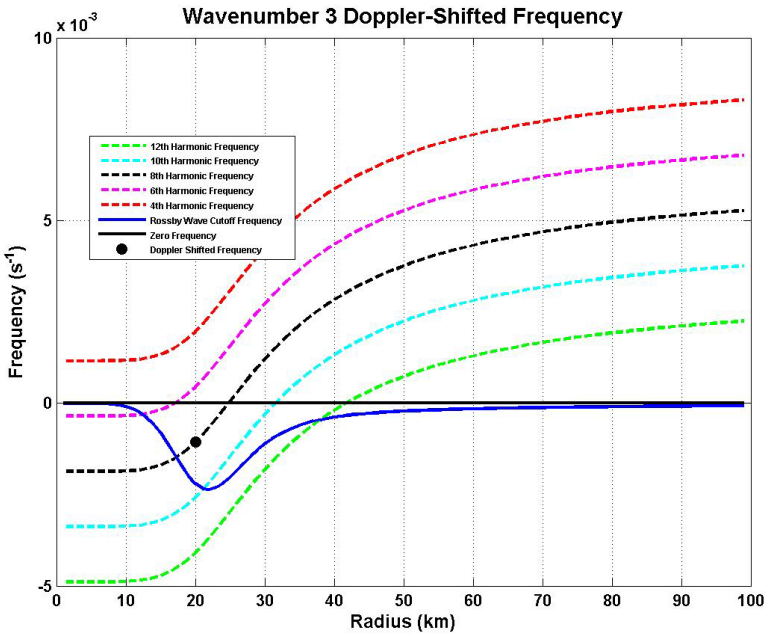

Figure 13: The Wavenumber 3 Doppler-Shifted frequency for harmonics 4, 6, 8, 10, and 12.

Harmonic 4, 6, 8, 10, and 12 Wavenumber 3 Solutions

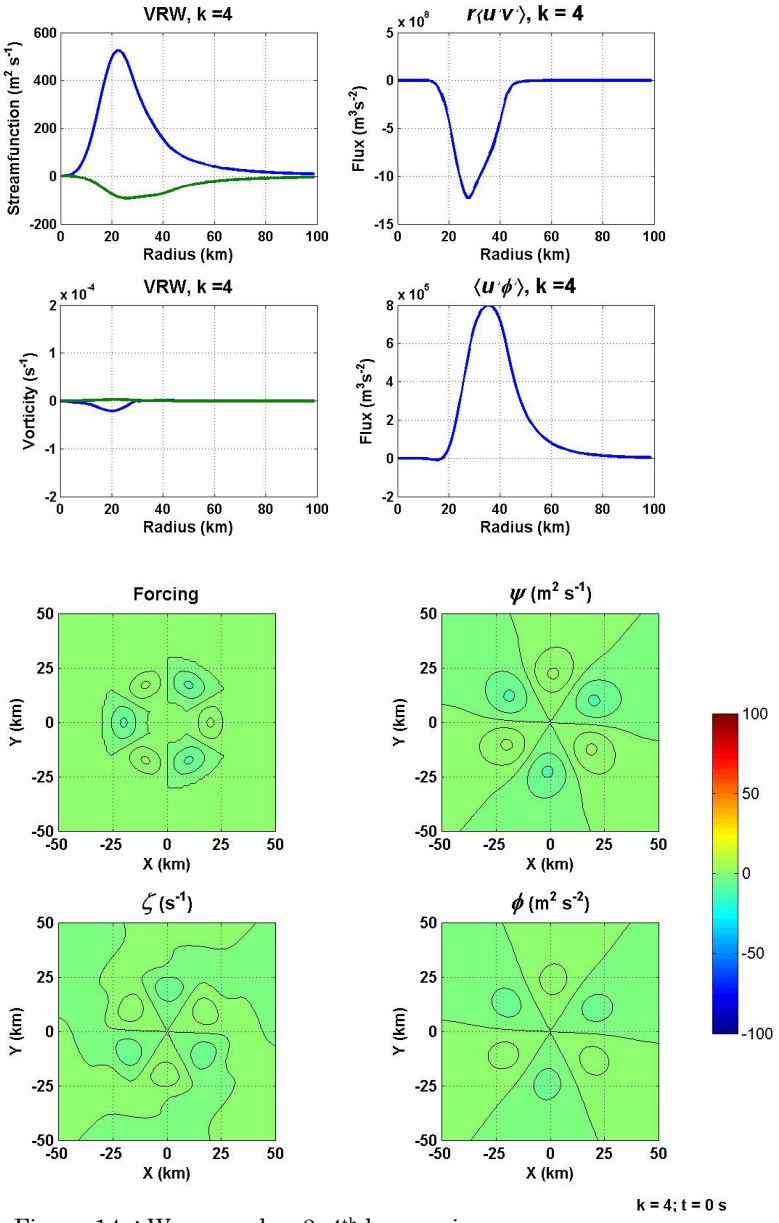

Figure 14a: Wavenumber 3, 4th harmonic.

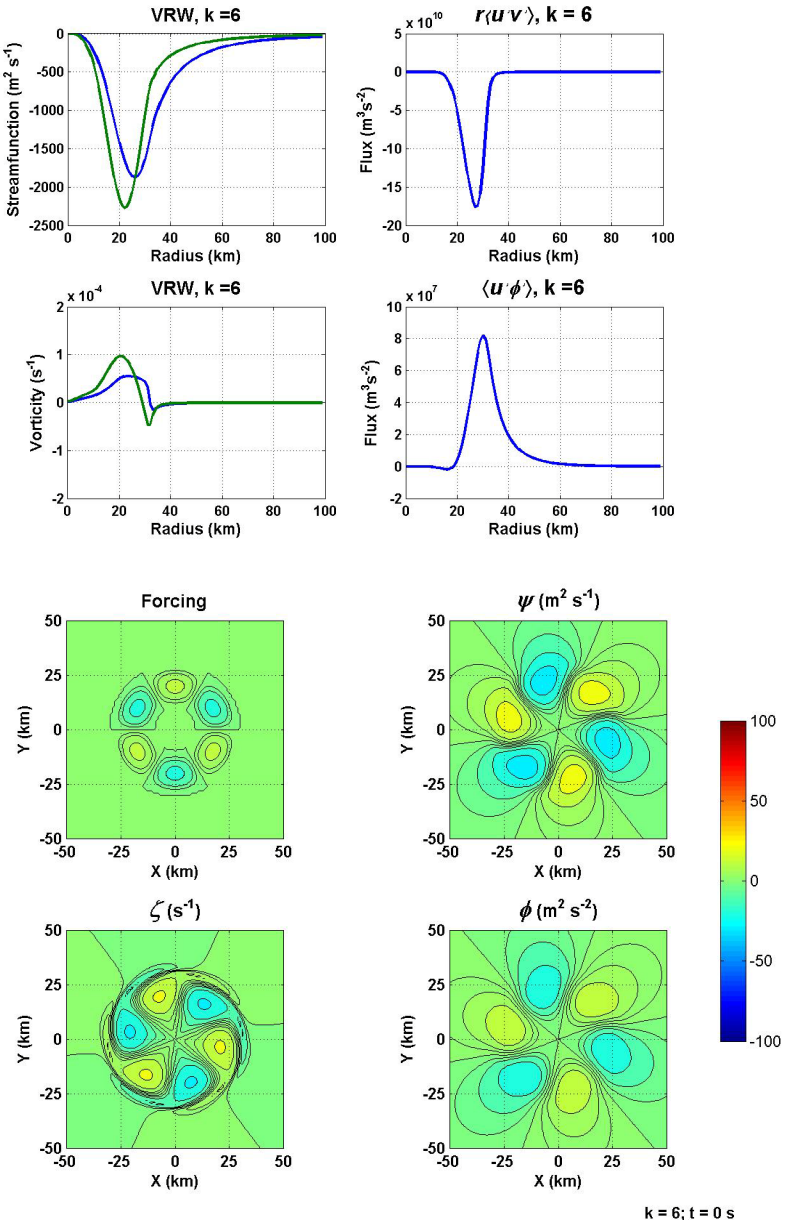

Figure 14b: Wavenumber 3, 6th harmonic.

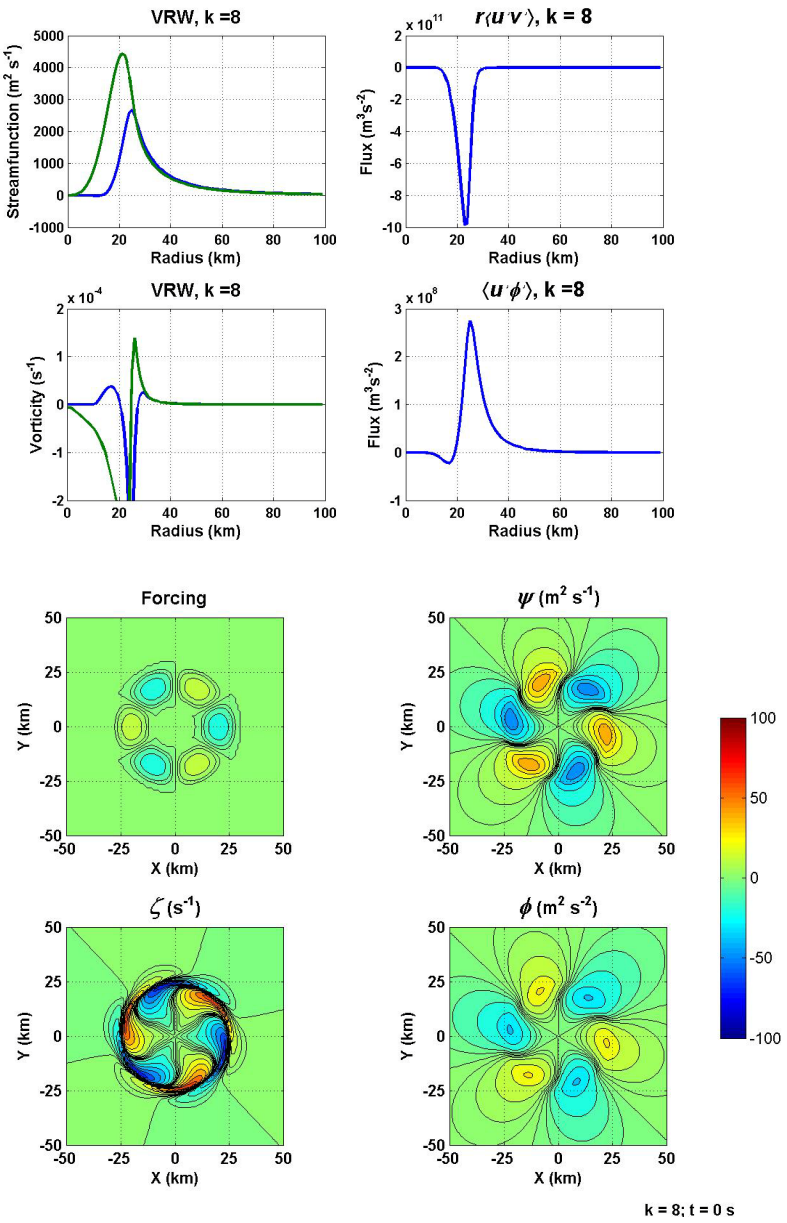

Figure 14c: Wavenumber 3, 8th harmonic.

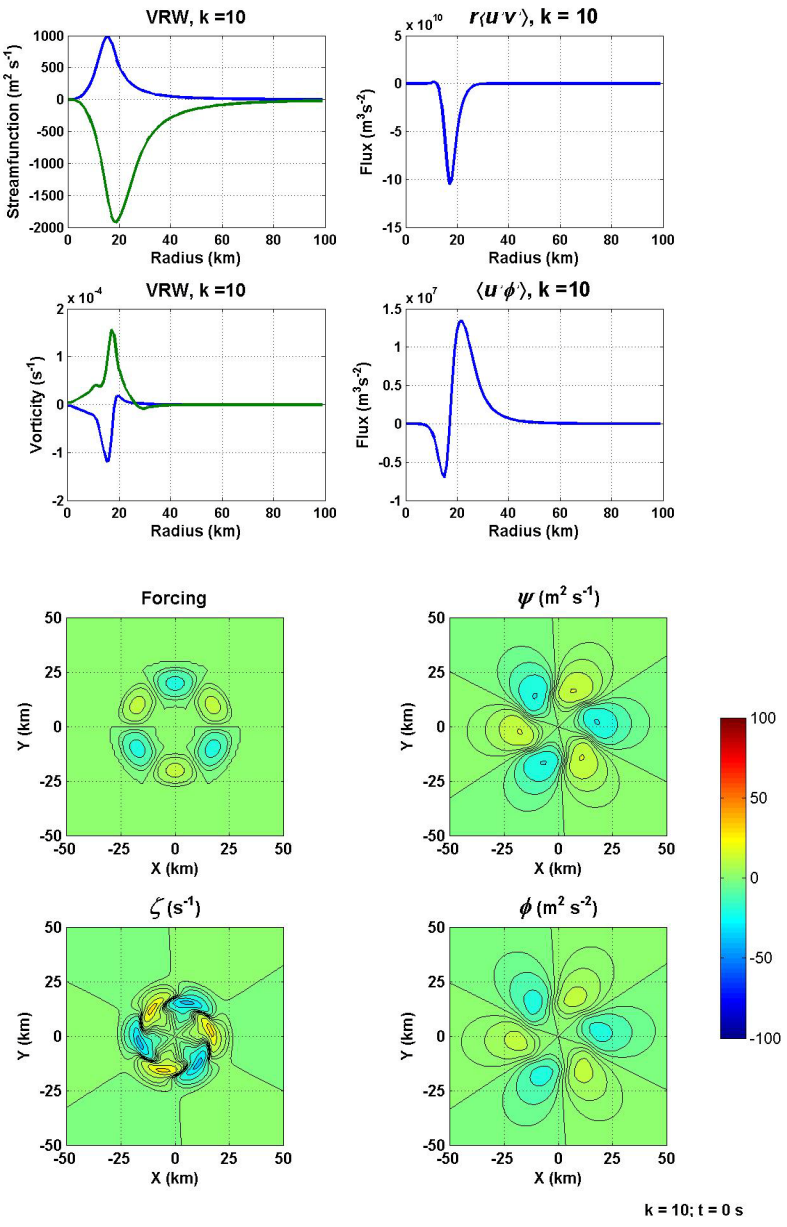

Figure 14d: Wavenumber 3, 10th harmonic.

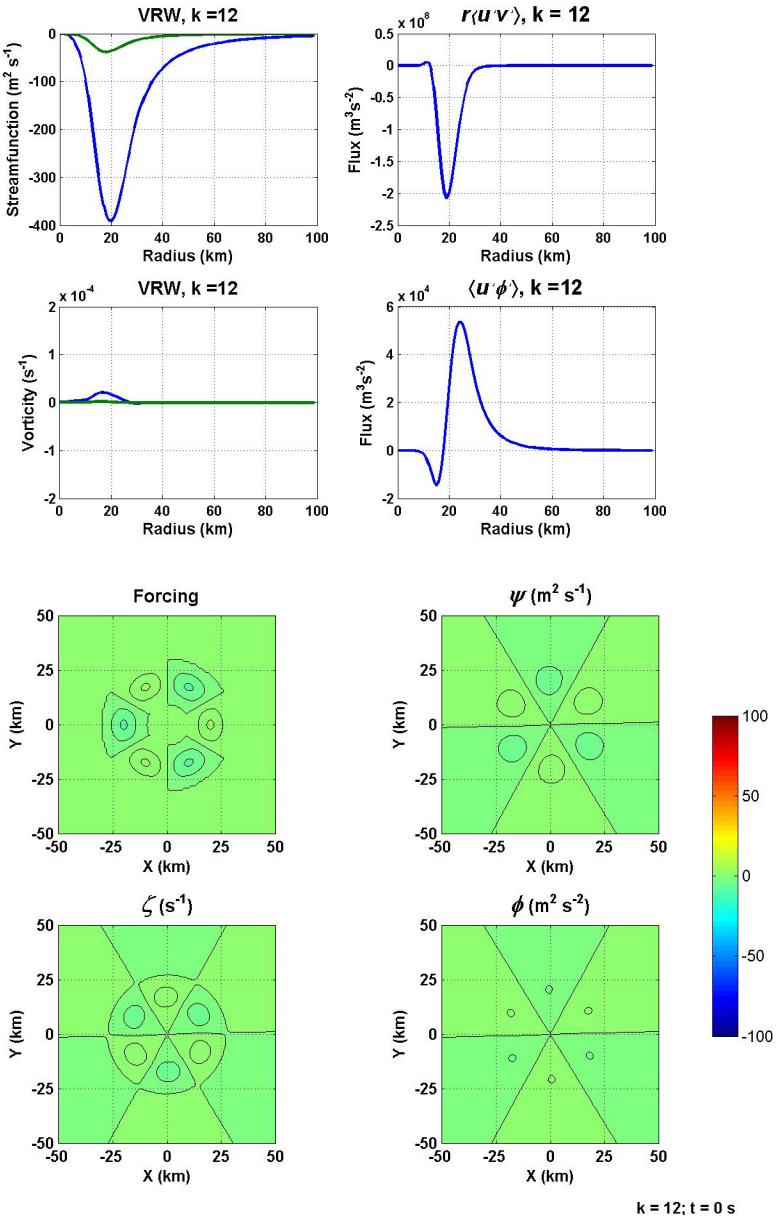

Figure 14e: Wavenumber 3, 12th harmonic.

Wavenumber 3 Forcing, Streamfunction, Vorticity, and Geopotential

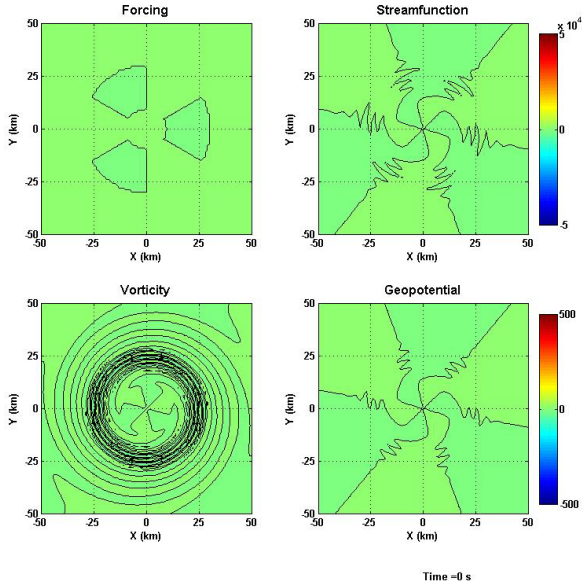

(a)

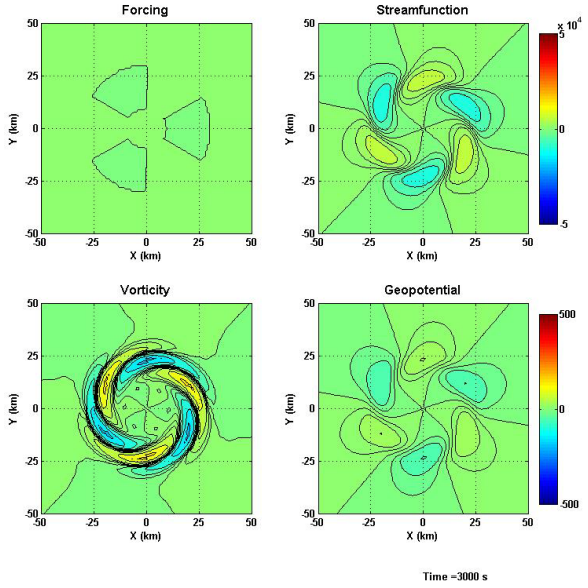

(b)

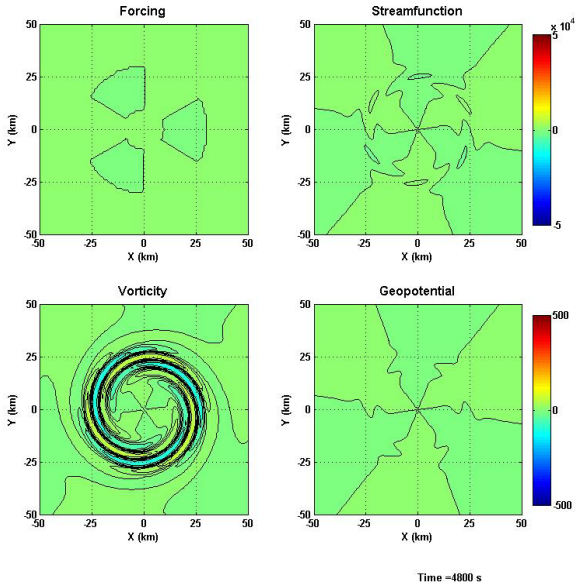

(c)

Figure 15: Wavenumber 3 forcing, streamfunction, vorticity, and geopotential for the complete solution at time (a) $t = 0$ s, (b) $t =$ 3000 s, and (c) $t = 4800$ s

In the wavenumber 4 solution (Figure 16) the ratio of the wave frequency to the wind's orbital frequency was raised to 0.90. Here, the maximum width of the waveguide is 10 km and only harmonics 8 and 10 fall within the frequency passband (Figures 17a-e). The 8th harmonic exhibits well-defined trailing spirals and vorticity filaments near the critical radius. The geopotential shows trailing spirals as well. The 6th harmonic has similar streamfunction and vorticity results; however, the frequency does not fall within the passband.

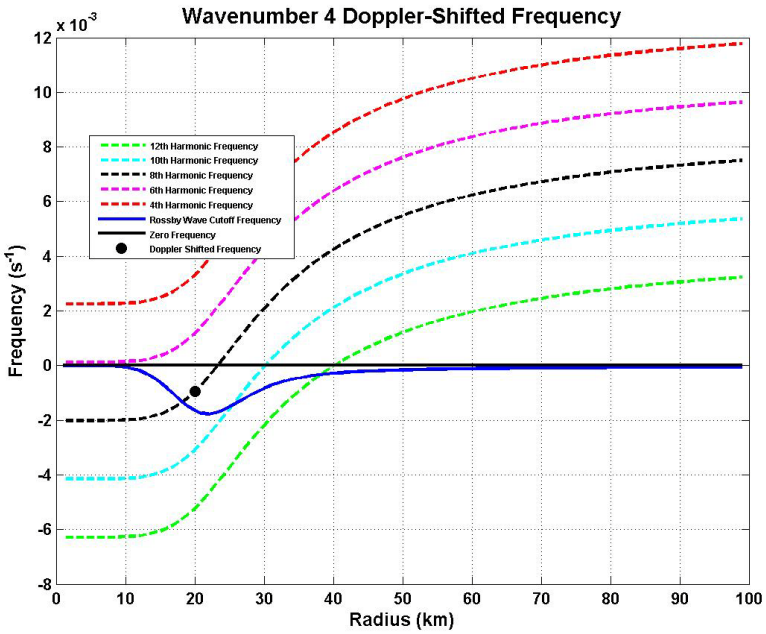

Figure 16: Wavenumber 4 Doppler-Shifted frequency for harmonics 4, 6, 8, 10, and 12.

Harmonic 4, 6, 8, 10, and 12 Wavenumber 4 Solutions

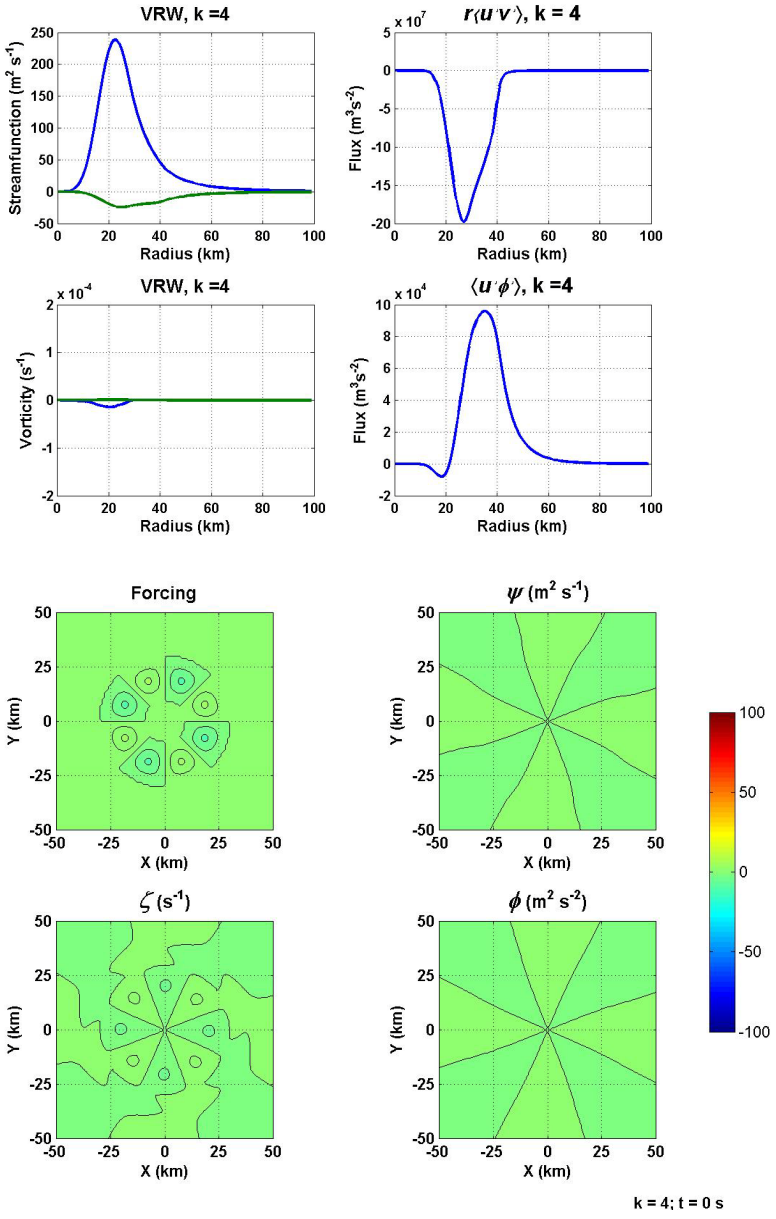

Figure 17a: Wavenumber 4, 4th harmonic.

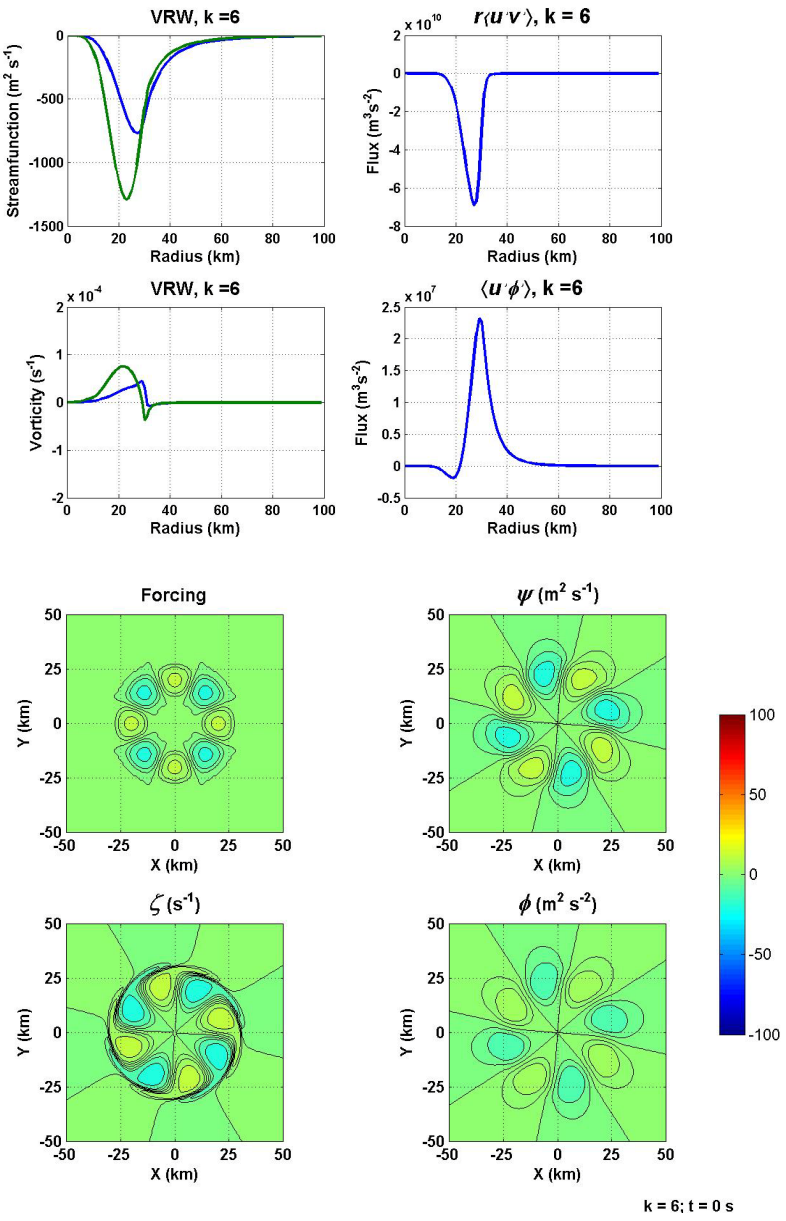

Figure 17b: Wavenumber 4, 6th harmonic.

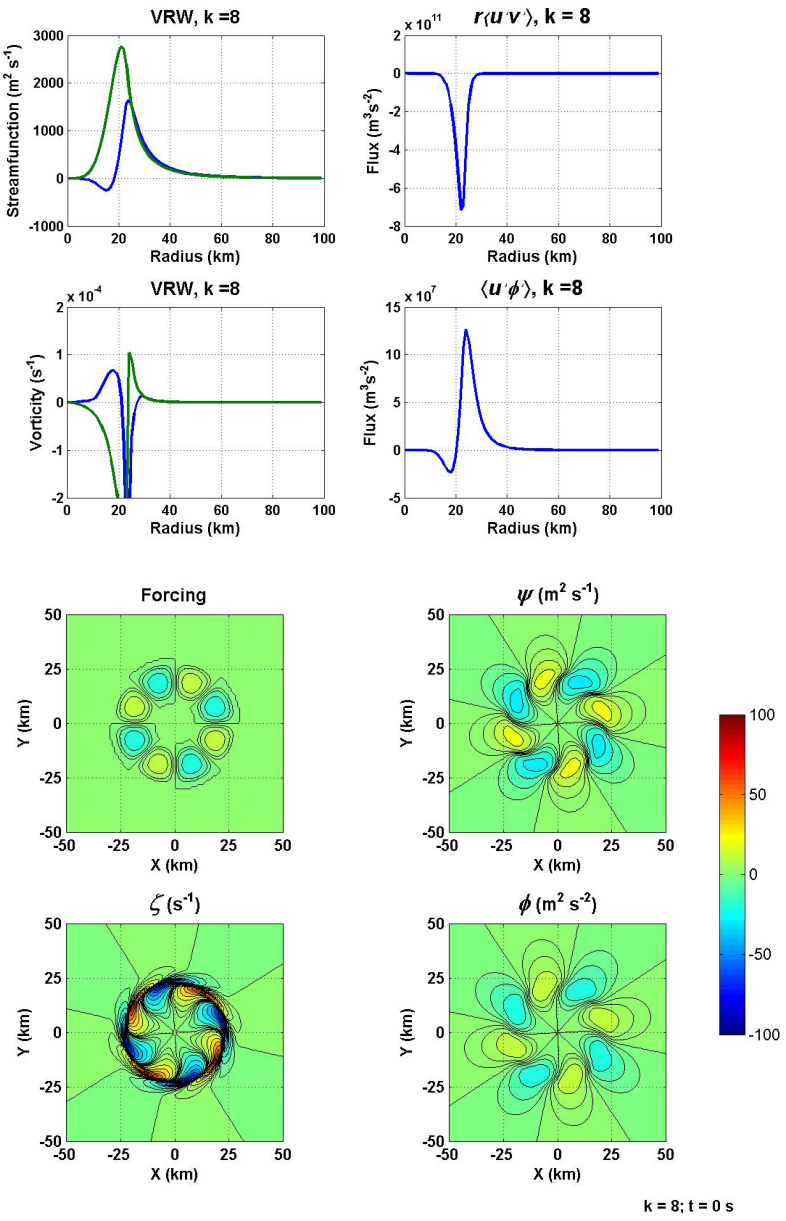

Figure 17c: Wavenumber 4, 8th harmonic.

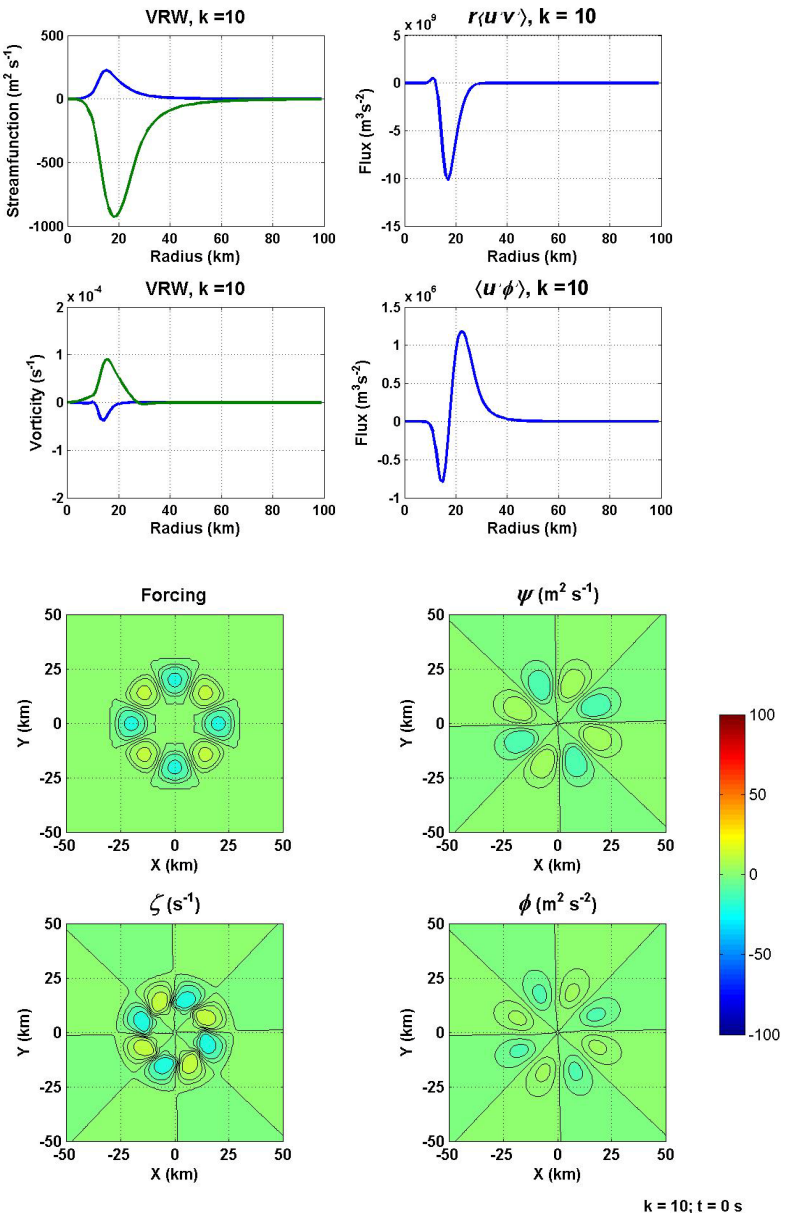

Figure 17d: Wavenumber 4, 10th harmonic.

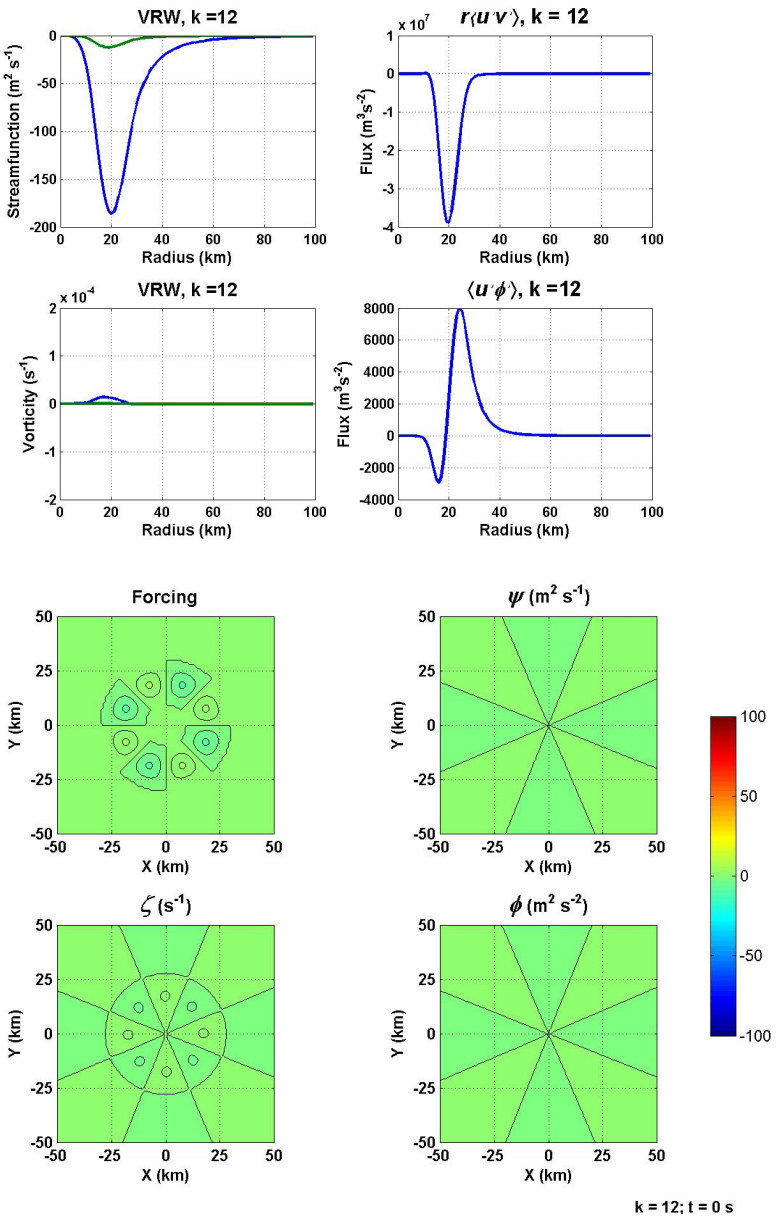

Figure 17e: Wavenumber 4, 12th harmonic.

Wavenumber 4 Forcing, Streamfunction, Vorticity and Geopotential

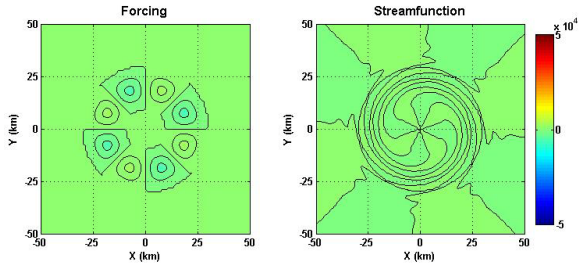

(a)

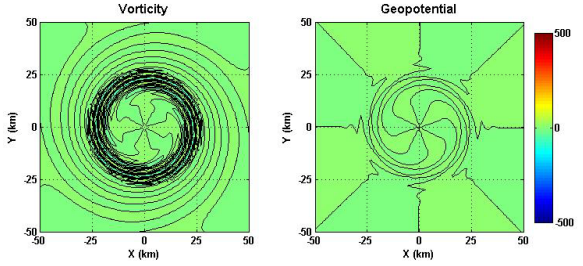

(b)

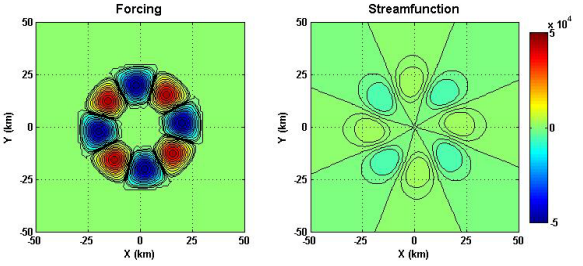

(c)

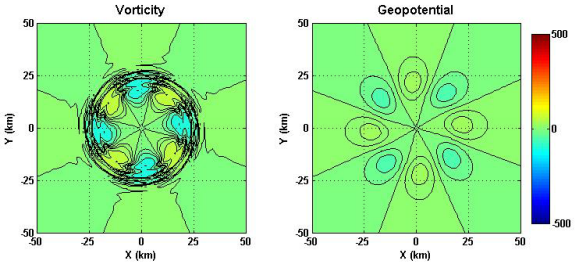

(d)

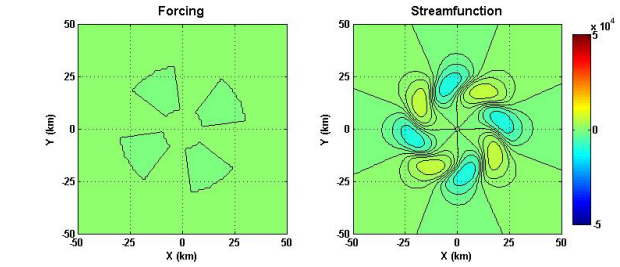

(e)

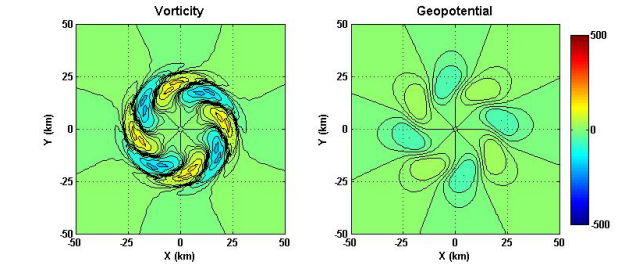

(f)

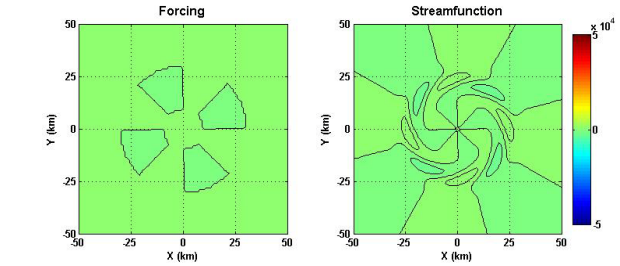

(g)

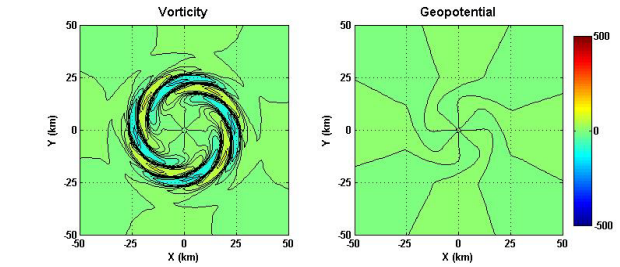

(h)

Figure 18: The forcing, streamfunction, vorticity, and geopotential for the complete solution of the wavenumber 4 forcing at time $t = 0$, 600, 1800, 3000 s.

The results in the wavenumbers 3 and 4 differ slightly in structure. The frequency needed to attain the widest possible waveguide becomes a larger fraction of the winds' orbital frequency and the width of the waveguides decrease with increasing tangential wavenumber. Of course, the numbers of distinct streamfunction and geopotential gyres increase even as the waveguide width decreases for higher wavenumbers.

In general, of the solutions, wavenumber 2 provides the most information and exhibits the most realistic properties. The wavenumber 2 has the strongest and best organized streamfunction and geopotential spirals and transports wave energy and angular momentum most effectively. The best simulation of the vorticity filamentation process was presented in the wavenumber 2 forcing as well.

CONCLUSIONS

Previous analysis of Vortex Rossby Waves (VRWs) used analytical solutions on idealized mean flows. The present results offer a straightforward numerical approach. The solutions are spiral-band like features that behave much like those observed in Tropical Cyclones, for example in Eastern Pacific Hurricane Olivia 1994.

The VRWs modeled here are vorticity waves induced by crudely modeled convection localized near the radius of maximum winds in a barotropic nondivergent, but otherwise hurricane-like vortex. They are advected downstream as a train of cyclonic and anticyclonic trailing spirals. Physically, they apparently correspond to observed spiral rain bands that rotate cyclonically around tropical cyclones with a speed slower than the mean swirling flow.

The Wavenumber 2 Non-divergent Barotropic Model captures much of the rotational dynamics of these bands when they are interpreted as Vortex Rossby waves. The present Fourier-series solutions, in contrast with previous models, simulate intermittent forcing, resulting in a more realistic solution that reveals the evolution of the waves as they propagate radially and their harmonics interfere constructively or destructively. The forcing includes no net symmetric forcing and, since the forcing is sinusoidal in time and azimuth, there is no net cyclonic vorticity induced. The forcing in the model is purely rotational consistent with barotropic, nondivergent dynamics.

Propagating waves can exist only in a frequency passband between the Rossby wave cut-off frequency and zero Doppler shifted frequency. Geometrically, this passband defines an annular waveguide with the forcing localized near its inner boundary. A fraction of the waves initially propagates inwards toward the center of the vortex. As it approaches the Rossby wave cut-off frequency, it is reflected and subsequently propagates outward. Both these waves and those that initially propagated outward are become filamented and are ultimately absorbed at the outer critical radius.

The wave momentum and geopotential fluxes are consistent with the Eliassen-Palm relation. Since the Doppler-shifted frequency is negative, they are oppositely directed. The waves transport net angular momentum inward and net wave energy outward. Angular momentum flux divergence near the critical radius decelerates the mean flow there and angular momentum convergence from the cut-off frequency radius to the locus of forcing accelerates the mean flow. The vorticity perturbations that accumulate near the critical radius stretch into narrow cyclonic and anticyclonic bands that become filamented as they wrap around the vortex. The structures of the corresponding streamfunction and geopotential gyres, however, are predominantly relatively broad trailing spirals and show less evident filamentation than the vorticity.

It is important to understand the relationship between VRWs and radial transports of angular momentum. This is the mechanism that determines how VRWs may cause vortex intensity changes. The Eliassen Palm theorem relates wave energy $\langle u\phi \rangle$ and angular momentum transports $r\langle uv \rangle$, where $\langle () \rangle$ denotes

azimuthal integration (Eliassen and Palm 1960). Vortex Rossby waves, propagating in their passband of negative frequencies, generally transport energy outward and angular momentum inward toward areas with large vorticity at and inside the radius of maximum winds. This mechanism in turn can lead to contraction of the eyewall and intensification. However, at the outer end of the waveguide where the Doppler shifted frequency approaches zero, filamentation and the vorticity masking of tightly wound spirals means that there is small net vorticity in the neighborhood of points in this region. Although VRW's can apparently influence intensity change for wavenumbers ≥ 2, their slow phase velocity limits their effect to a narrow radial interval generally outward from the locus of forcing.

LIST OF REFERENCES

Andrews, D. G., M. E. McIntyre, 1976a: Planetary Waves in Horizontal and Vertical Shear: The Generalized Eliassen-Palm Relation and the Mean Zonal Acceleration. *J. Atmos. Sci.*, **33**, 2031–2048. DOI: 10.1175/1520-0469(1976)033<2031:PWIHAV>2.0.CO;2

Andrews, D. G., M. F. McIntyre, 1976b: Planetary Waves in Horizontal and Vertical Shear: Asymptotic Theory for Equatorial Waves in Weak Shear. *J. Atmos. Sci.*, **33**, 2049–2053. DOI: 10.1175/1520-0469(1976)033<2049:PWIHAV>2.0.CO;2

Black, M.L., J.F. Gamache, F.D. Marks, Jr, C.E. Samsury, and H.E.Willoughby, 2002: Eastern–Pacific Hurricanes Jimena of 1991 and Olivia of 1994: The effects of vertical shear on structure and intensity. *Mon. Wea. Rev.*, **130**, 2291-2312.

Boyd, John P., 1976: The Noninteraction of Waves with the Zonally Averaged Flow on a Spherical Earth and the Interrelationships on Eddy Fluxes of Energy, Heat and Momentum. *J. Atmos. Sci.*, **33**, 2285–2291. DOI: 10.1175/1520-0469(1976)033<2285:TNOWWT>2.0.CO;2

Chen, Yongsheng and M.K. Yau, 2001: Spiral Bands in a Simulated Hurricane. Part I: Vortex Rossby Wave Verification. *J. Atmos. Sci.*, **58**, 2128-2145.

Chen, Yongsheng, G. Brunet, and M.K. Yau, 2003: Spiral Bands in a Simulated Hurricane. Part II: Wave Activity Diagnostics. *American Meteor. Soc.*, **60**, 1239-1256.

Churchill, R. V.: "Fourier Series and Boundary Value Problems," 2nd ed. McGraw-Hill Book Company, Inc., New York, 1963.

Corbosiero, K.L., J. Molinari, and M.T. Black, 2005: The Structure and Evolution of Hurricane Elena (1985). Part I: Symmetric Intensification. *American Meteor. Soc.*, **133**, 2905-2921.

Corbosiero, K.L., J. Molinari, A.R Aiyyer, and M.L. Black, 2006: The Structure and Evolution of Hurricane Elena (1985). Part II: Convective Asymmetries and Evidence for Vortex Rossby Waves. *American Meteor. Soc.*, **134**, 3073-3091.

Eliassen, A., 1952: Slow Thermally or Frictionally Controlled Meridional Circulation in a Circular Vortex. *Astrophys. Norv.* **5**, 19-60.

Eliassen, A. and E. Palm, 1960: On the Transfer of Energy in Stationary Mountain Waves. *Geofysiske Publikasjoner Geophysica Norvegica*, **XXII (3)**, 1-23.

Guinn, T.A., and W.H. Schubert, 1993: Hurricane Spiral Bands. *J. Atmos. Sci.*, **50 (20)**, 3380-3403.

Hendricks, E. A., M. T. Montgomery, and C. A. Davis, 2004: The role of "Vortical" Hot Towers in the Formation of Tropical Cyclone Diana (1984). *J. Atmos. Sci.*, **61**, 1209-1232.

Houze J.R., R.A., 2010: Clouds in Tropical Cyclones. *Mon. Wea. Rev.*, **138**, 293-344. DOI: 10.1175/2009MWR2989.1

Judt, F., and S.S. Chen, 2010: Convectively Generated Potential Vorticity in Rainbands and Formation of the Secondary Eyewall in Hurricane Rita of 2005. *American Meteor. Soc.*, **67**, 3581-3599. DOI: 10.1175/2010JAS3471.1

Kossin, J.P., W.H. Shubert, M.T. Montgomery, 2000: Unstable Interactions between a Hurricane's Primary Eyewall and a Secondary Ring of Enhanced Vorticity. *J. Atmos. Sci.*, **57**, 3893-3917.

Lindzen, R.S., and H.L. Kuo, 1969: A Reliable Method for the Numerical Integration of a Large Class of Ordinary and Partial Differential Equations. *Mon. Wea. Rev.*, **97 (10)**, 732-734.

MacDonald, N.J., 1968: The Evidence for the Existence of Rossby-like Waves in the Hurricane Vortex. *Tellus XX (196S)*, **1**, 138-150.

McIntyre, M. E. 1977: Wave transport in stratified rotating fluids. *Springer Lecture Notes in Physics*, **7 1**, 290-3 14.

Möller, J. D., and M. T. Montgomery, 1999: Vortex Rossby waves and Hurricane Intensification in a Barotropic Model. *J. Atmos. Sci.,* **56,** 1674-1687.

Möller, J. D., and M. T. Montgomery, 2000: Tropical Cyclone Evolution via Potential Vorticity Anomalies in a Three-Dimensional Balance Model. *J. Atmos. Sci.,* **57**, 3366-3387.

Montgomery, M. T., and R. J. Kallenbach, 1997: A Theory for Vortex Rossby Waves and its Application to Spiral Bands and Intensity Changes in Hurricanes. *Quart. J. Roy. Meteor. Soc.*, **123**, 435-465.

Montgomery, M. T., and J. Enagonio, 1998: Tropical cyclogenesis via convectively forced vortex Rossby waves in a three-dimensional quasigeostrophic model. *J. Atmos. Sci.*, **55**, 3176-3207.

Montgomery, M.T, M.E. Nicholls, T.A. Cram, and A.B. Saunders, 2006: A Vortical Hot Tower Route to Tropical Cyclogenesis. *American Meteor. Soc.*, **63**, 355-386.

Nguyen, C. M., M.J. Reeder, N.E Davidson, R.K. Smith, and M.T. Montgomery, 2010: Inner Core Vacillation Cycles during the Intensification of Hurricane Katrina. *Quart. J. Roy. Meteor. Soc.*, **00**, 2-16.

Nolan, D.S. and M.T. Montgomery, 2002: Nonhydrostatic, Three-Dimensional Perturbations to Balanced, Hurricane-like Vortices. Part I: Linearized Formulation, Stability, and Evolution. *J. Atmos. Sci.*, **59 (21)**, 2989-3020.

Nolan, D.S. and L.D. Grasso, 2003: Nonhydrostatic, Three-Dimensional Perturbations to Balanced, Hurricane-Like Vortices. Part II: Symmetric Response and Nonlinear Simulations. *J. Atmos. Sci.*, **60 (22)**, 2717-2745.

Nolan, D.S., Y. Moon, and D.P. Stern, 2007: Tropical Cyclone Intensification from Asymmetric Convection: Energetics and Efficiency. *J. Atmos. Sci.*, **64**, 3377-3405. DOI: 10.1175/JAS3988.1

Painemal, David. "Eliassen-Palm Theory." *MPO611*: 1-14. Rosenstiel School of Marine and Atmospheric Science. Web. 26 Oct 2011.

Pendergrass, A.G. and H.E. Willoughby, 2009: Diabatically Induced Secondary Flows in Tropical Cyclones. Part I: Quasi-Steady Forcing. *Mon. Wea. Rev.*, **137**, 805-821.

Qiu, X., Z. Tan, and Q. Xiao, 2010: The Roles of Vortex Rossby Waves in Hurricane Secondary Eyewall Formation. *Mon. Wea. Rev.*, **138**, 2092–2109. DOI: 10.1175/2010MWR3161.1.

Reasor, P.D., M.T. Montgomery, F.D. Marks J.R., and J.F. Gamache, 2000: Low-Wavenumber Structure and Evolution of the Hurricane Inner Core Observed by Airborne Dual-Doppler Radar. *American Meteor. Soc.*, **128**, 1653-1680.

Romine, G.S. and R.B. Wilhelmson, 2006: Finescale Spiral Band Features within a Numerical Simulation of Hurricane Opal (1995). *American Meteor. Soc.*, **134**, 1121-1139.

Schubert, W.H. and J.J. Hack, 1982: Inertial Stability and Tropical Cyclone Development. *American Met. Soc.*, **39**, 1687-1697.

Senn, H. V., and H. W. Hiser, 1959: On the Origin of Hurricane Spiral Bands. *J. Meteor.,* **16,** 419–426.

Shapiro, L. and H.E. Willoughby, 1982: The Response of Balanced Hurricanes to Local Sources of Heat and Momentum. *J. Atmos. Sci.*, **39**, 378-394.

Shapiro, L.J., and M.T. Montgomery, 1993: A Three-Dimensional Balance Theory for Rapidly Rotating Vortices. *J. Atmos. Sci.*, **50 (19)**, 3322-3335.

Terwey, W.D. and M.T. Montgomery, 2002: Wavenumber-2 and Wavenumber-*m* Vortex Rossby Wave Instabilities in a Generalized Three-Region Model. *American Met. Soc.*, **59**, 2421-2427.

Willoughby, H.E., 1977: Inertia-Buoyancy Waves in Hurricanes. *J. Atmos. Sci.*, **34**, 1028-1039.

Willoughby, H.E., 1978: A Possible Mechanism for the Formation of Hurricane Rainbands. *J. Atmos. Sci.*, **35**, 838-848.

Willoughby, H.E., 1988: The Dynamics of the Tropical Cyclone Core. *Aust. Meteor. Mag.,* **36,** 183–189.

Willoughby, H.E., F.D. Marks, and R. J. Feinberg, 1984: Stationary and Moving Convective Bands in Hurricanes. *J. Atmos. Sci.*, **41**, 3189–3211. DOI: 10.1175/1520-0469(1984)041<3189:SAMCBI>2.0.CO;2.

Willoughby, H.E., E.N. Rappaport, and F. D. Marks, 2007: Hurricane Forecasting: The State of the Art. *Natural Hazards Review*. **8**, 45-49.

APPENDIX

Comparison with Observed Spiral Bands

NOAA's WP-3D research aircraft, N42RF and N43RF, observed Hurricane Olivia on 24 and 25 of September 1994. The evolution of Olivia's vortex was controlled by shear, abortive formation of a concentric outer eyewall, and motion over decreasing ocean surface temperatures.

Convectively induced spiral bands in and just outside Olivia's eyewall had a gret deal in common with the VRWs simulated here. Radar echoes and updrafts rotated around the vortex within 60-80% of the tangential mean wind (Figures A4 and A5). Convection was organized as axisymmetric rings during times of weak shear. In stronger shear, asymmetric convection was localized in convergence on the downshear side of the eye and subsequently rotated cyclonically around it. Since the cells' intensity fluctuated, they were relatively short lived. The updrafts rotating near the eye reached their maximum reflectivity on the left side of the shear direction and dissipated up-shear of the center.

The Intermittently Forced Vortex Rossby waves' wavenumber 2 forcing was designed to simulate these features. As shown in Figures A4 and A5, the forcing rotates at 60% of the mean tangential wind speed of 50 ms^{-1}, similar to the speed of the spiral rain bands in Olivia. The locus of the forcing is at and inward from the wind maximum. This geometry is parallel that of Olivia's strong convective updrafts.

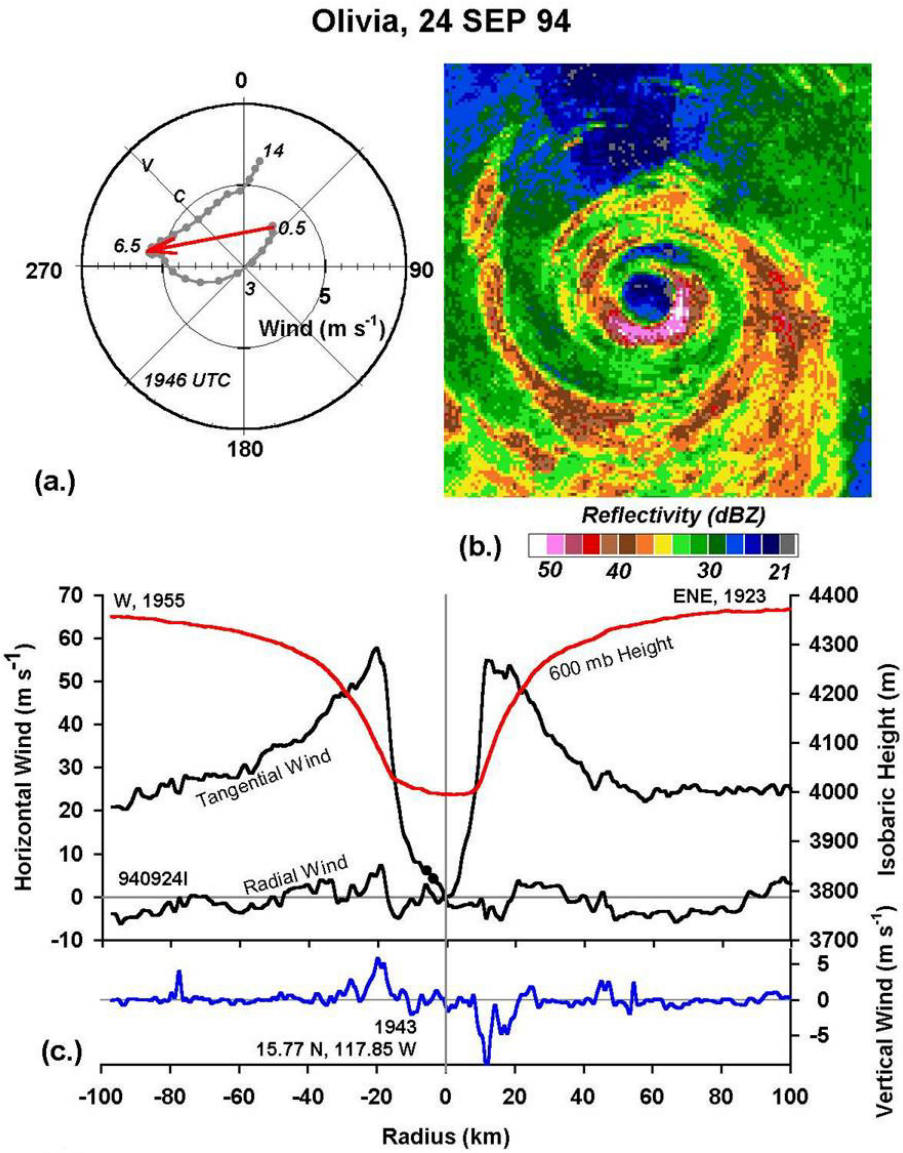

Figure A1: Hurricane Olivia on 24 Sep 1994; (a) Doppler-determined relative-wind holograph, storm motion, and earth-relative vertically averaged wind at 1946 UTC. (b) A 240 X 240 km PPI composite for 1934-1956 UTC. (c) A profile of flight-level observations by N42RF on an east-northeast-to-west pass across the center at 600 hPa, 1923-1955 UTC (Black et al. 2002).

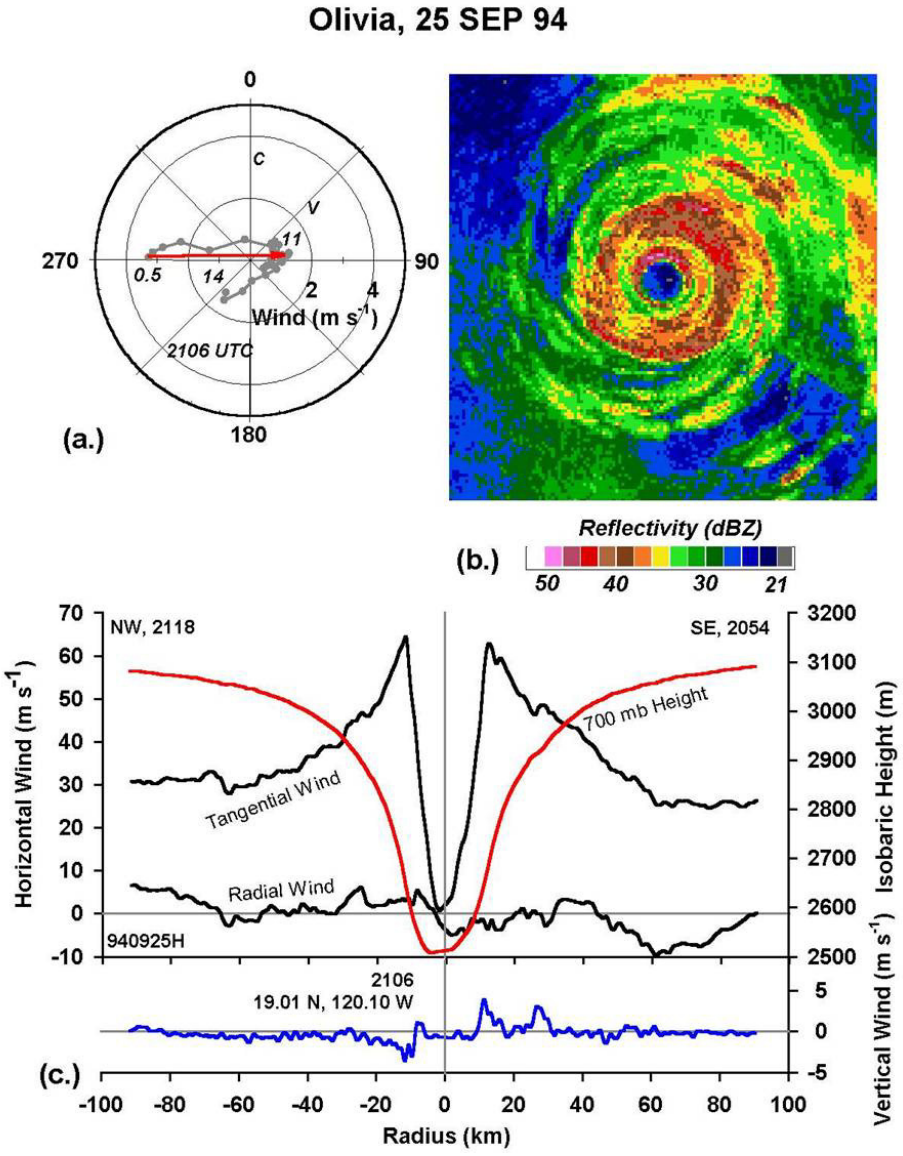

Figure A2: Hurricane Olivia on 25 Sep 1994; (a) Doppler-determined relative-wind holograph, storm motion, and earth-relative vertically averaged wind at 2106 UTC. (b) A 240 X 240 km PPI composite for 2054-2117 UTC. (c) A profile of flight-level observations by N42RF on south-to-northwest pass across the center at 700 hPa, 2054-2118 UTC (Black et al. 2002).

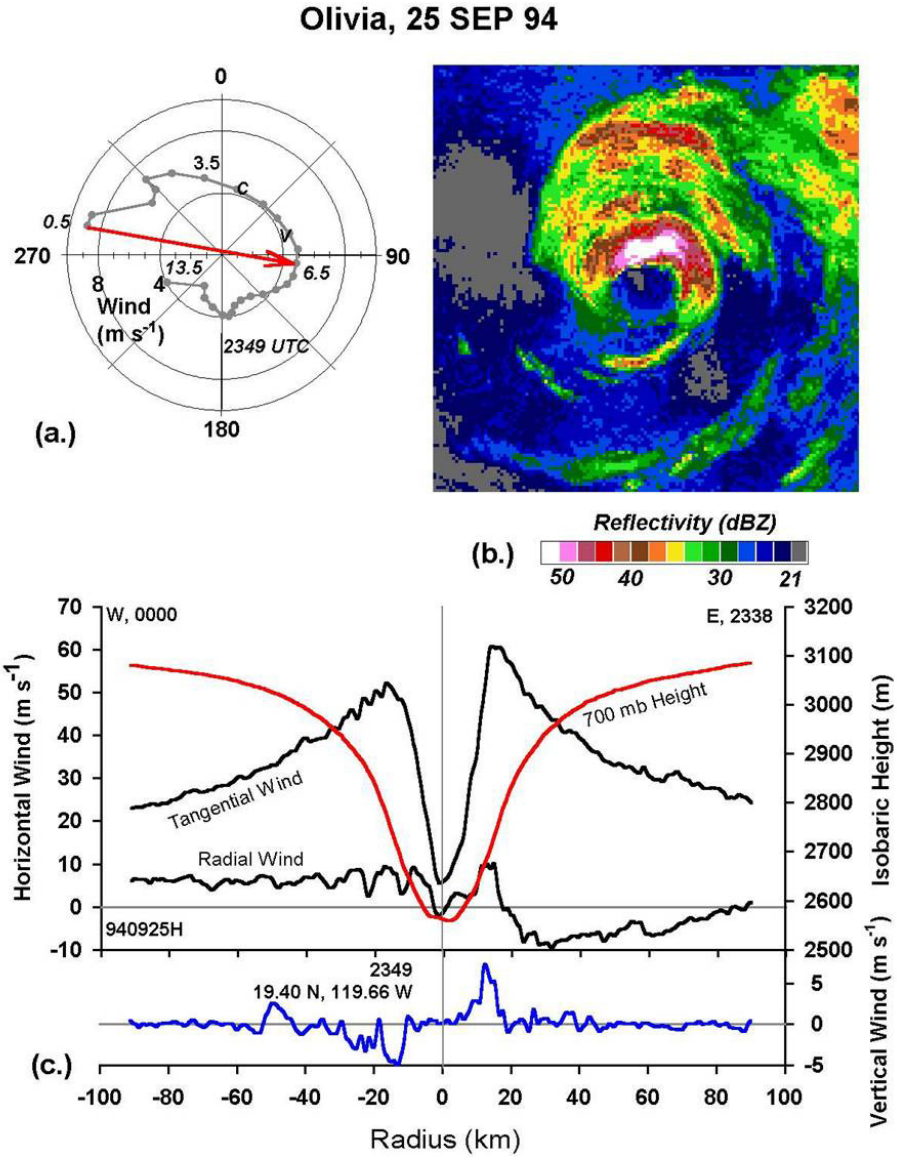

Figure A3: Hurricane Olivia on 25 Sep 1994; (a) Doppler-determined relative-wind holograph, storm motion, and earth-relative vertically averaged wind at 2349 UTC. (b) A 240 X 240 km PPI composite for 2338-2359 UTC. (c) A profile of flight-level observations by N42RF on an east-to-west pass across the center at 700 hPa, 2338-0000 UTC (Black et al. 2002).

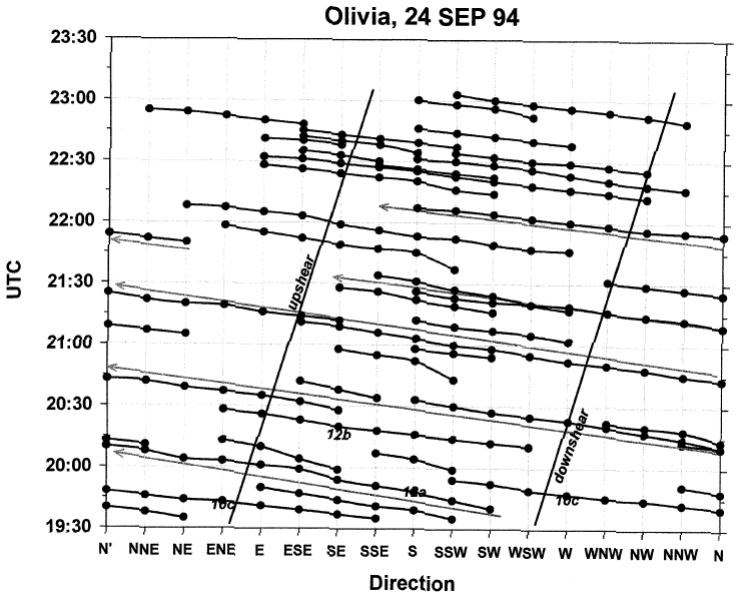

Figure A4: Hurricane Olivia on 24 Sep 1994; Time-azimuth plots of individual convective cells in Olivia's eyewall from 1935-2304 UTC on 24 Sept 1994 (Black et al. 2002).

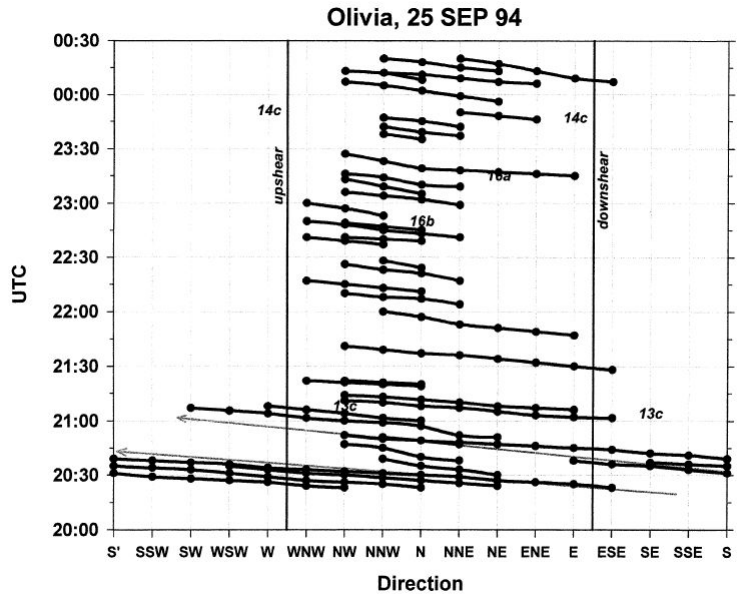

Figure A5: Hurricane Olivia on 25 Sep 1994; Time-azimuth plots of individual convective cells in Olivia's eyewall from 2023-0024 UTC on 25 Sept 1994 (Black et al. 2002).